Bachelor's Thesis

Characterisation of MAPS Prototypes for the ALICE 3 Outer Tracker

Omar Mohamed Ahmed Fouad Yousef Abdelrahman

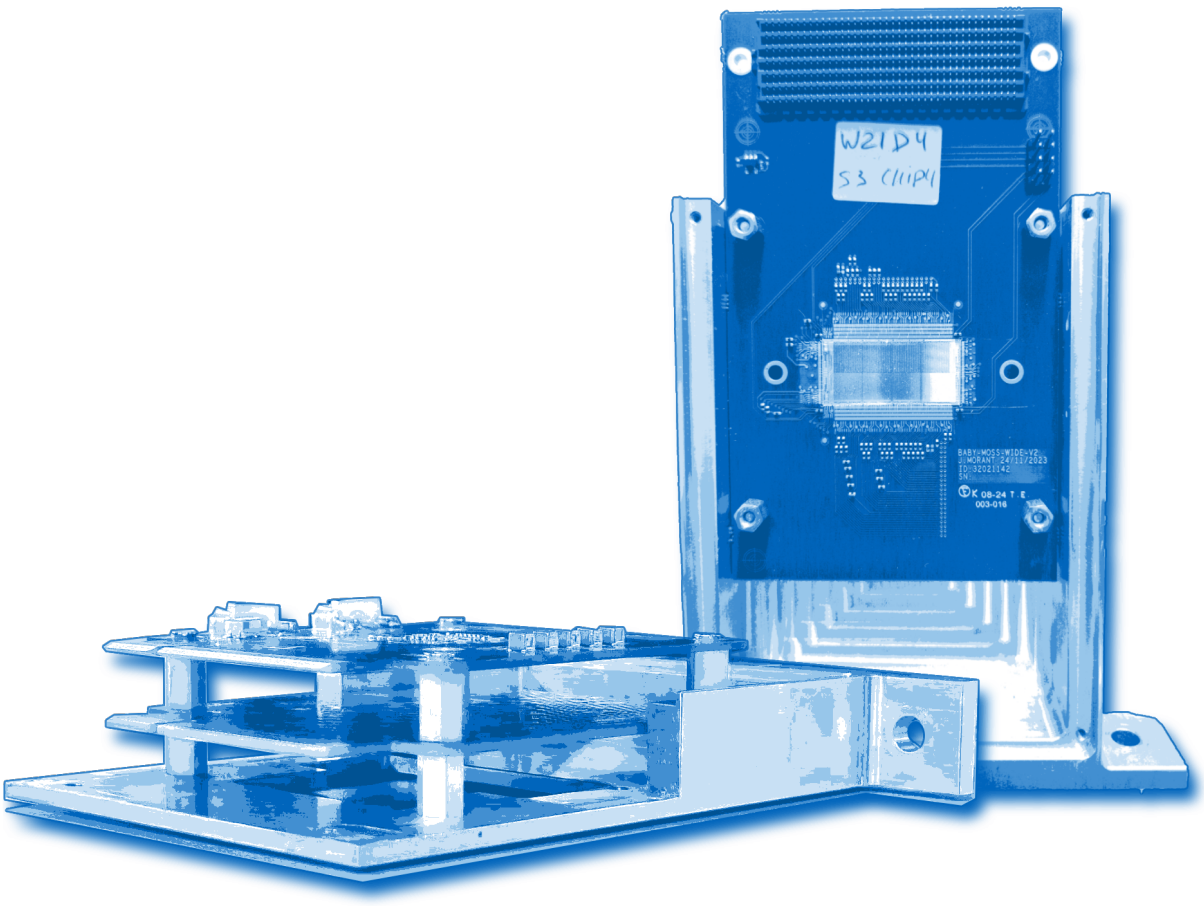

TECHNISCHE UNIVERSITÄT MÜNCHEN

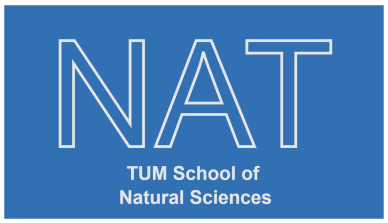

Characterisation of MAPS Prototypes for the ALICE 3 Outer Tracker

Charakterisierung von MAPS Prototypen für den ALICE 3 Outer Tracker

Bachelor's Thesis

Author: Omar Mohamed Ahmed Fouad Yousef Abdelrahman
Examiner: Prof. Dr. Laura Fabbietti
Supervisor: Henrik Fribert
Date: September 17, 2025

Disclaimer

I confirm that the results presented in this bachelor's thesis are my own work and that I have documented all sources and materials used.

Ich versichere, dass ich diese Bachelorarbeit selbstständig verfasst und nur die angegebenen Quellen und Hilfsmittel verwendet habe.

Munich, September 17, 2025 Omar Mohamed Ahmed Fouad Yousef Abdelrahman

Abstract

Monolithic Active Pixel Sensors (MAPS), based on CMOS imaging technology, are an integral part of modern pixel tracking detectors. The ALICE experiment at the LHC implements this technology in its Inner Tracking System (ITS), and the upcoming ITS3 upgrade will make even fuller use of MAPS. In the near future, the ALICE 3 experiment will expand this approach to an unprecedented active area of approximately $60\,\mathrm{m}^2$, with tracking performed entirely using CMOS MAPS sensors.

Given the large area, it is advantageous for power consumption and readout to reduce the total number of pixels by employing large-pitch sensors in the outer tracker layers, where spatial resolution requirements are more relaxed. However, it is not yet clear how large a pixel can be implemented in 65 nm CMOS MAPS technology without compromising detection efficiency, particularly in the pixel corners and under irradiation. To address this question, large-pitch pixel prototypes will be produced next year and studied in dedicated test setups.

This work investigates the characteristics of two types of MAPS detectors, the APTS and BabyMOSS, with measurements performed both in the laboratory and at the DESY test beam facility. Laboratory measurements were carried out using DAQ boards with integrated FPGAs connected to the chips via proximity or carrier cards and intermediate raiser boards, allowing systematic studies under controlled conditions. For the test beam, multiple layers of these setups were installed in a telescope configuration to evaluate detector performance in a realistic particle beam environment. For BabyMOSS, studies included varying thresholds and angles with respect to the beam, while for the APTS, measurements were taken at different back-bias voltages.

Analysis of the combined laboratory and test beam data allowed determination of optimal operational parameters through threshold and fake-hit-rate studies, which were then applied to the beam data. The test beam results showed that angled detector setups yielded higher efficiency than flat configurations, and lower thresholds further improved efficiency. For the APTS, higher back biases increased efficiency by strengthening the electric field in each pixel. Limited statistics prevented precise spatial resolution measurements for the APTS, but the observed trends largely confirmed prior expectations.

Finally, this thesis demonstrates the functionality of the BabyMOSS-based telescope and develops the pipeline required for the analysis of both laboratory and test beam data. The insights obtained here will be directly useful for the study and optimization of future large-pitch MAPS detectors, such as those intended for ALICE 3.

Contents

1 Introduction

1.1 MAPS

In high-energy physics (HEP), silicon semiconductor detectors are widely used. Their operation relies on the drift and diffusion of charge carriers, namely electrons and holes, which are created in pairs when a charged particle traverses the active volume of the silicon lattice, the epitaxial layer. To enable charge collection, regions of the silicon are selectively doped with donor and acceptor atoms, forming *pn-junctions*. Under reverse bias, a depletion region develops across the epitaxial layer, providing the active volume of the detector. Charge carriers generated within this region are separated by the electric field and drift towards their respective collection electrodes, where the signal is registered. To this end, one must have readout electronics connected to each pixel.

Monolithic Active Pixel Sensors (MAPS) are silicon-based semiconductor sensors. *"Monolithic"* describes the fact that all readout electronics are placed on each pixel, simplifying the readout process and removing the necessity for intermediate connection methods between the sensing diodes and the electronics, as is the case with hybrid pixels with integrated bump bonds [1]. The term *"Active"* refers to there being an active transistor on each pixel. For MAPS usage in HEP, CMOS (Complementary Metal–Oxide–Semiconductor) technology is implemented, a production method for integrated circuitry [2],[3].

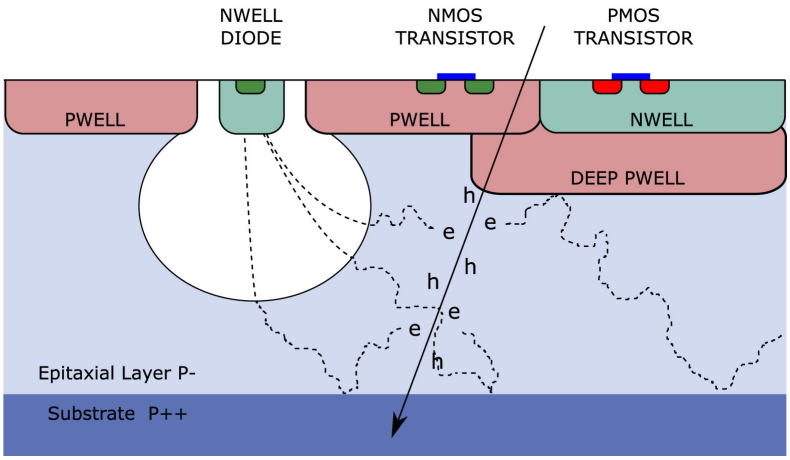

Figure 1.1: Cross-section of a MAPS pixel. The figure shows the diffusion of the charge carriers towards the depletion region (white). [4]

The MAPS approach offers several advantages for particle tracking in HEP experiments. The monolithic design reduces material budget by eliminating bump bonds and

separate readout ASICs, which is critical for minimizing multiple scattering in tracking detectors. CMOS technology allows for high granularity and excellent spatial resolution while keeping power consumption low. Furthermore, the industrial availability of CMOS processes makes MAPS cost-efficient and scalable, enabling large-area detector assemblies.

1.2 ALICE

A Large Ion Collider Experiment (ALICE) [5] at the LHC is a detector experiment focusing on investigating Quark-Gluon-Plasma (QGP), which is theorised to have existed in the early stages of the universe after the Big Bang, by studying the strong interactions between particles under extreme conditions, similar to those thought to have existed after the Big Bang. To this end, ultra-relativistic heavy ion collisions at the LHC (most notably Pb-Pb), which produce such high temperatures and energy densities, are investigated. In the state of QGP, quarks and gluons are not confined in hadrons anymore, but are able to strongly interact in a nearly perfect fluid, according to the laws of quantum chromodynamics (QCD). By detecting and studying the characteristics of the hadrons, leptons, and heavy-flavour quarks produced in such collisions, the QGP can be studied.

ALICE is based on multiple state-of-the-art tracker detectors. The innermost part of the detector, directly covering the collision point, is the Inner Tracking System (ITS) [6]. The ITS will be discussed in more detail in Section 1.2.1. In conjunction with the Time Projection Chamber (TPC) [7], high-accuracy tracks of the ionising particles can be reconstructed. The TPC utilises Gas Electron Multiplier (GEM) [8] detectors to perform tracking as the charges drifting from the ionisation are collected at the electrodes, projecting the track of the particle in the plane. The time difference between the ionisation and the detection can be used to measure the position in the z coordinate, providing sufficient information for tracking when combined with the information from the ITS. In the TPC, particle identification (PID) can be performed by measuring the specific energy loss (Bethe-Bloch, dE/dx) [9] of the particles as they ionise the gas inside the chamber, which is dependent on the charge and velocity of the particle. Both the

1.2.1 ITS2 and ITS3

ITS2 is the Inner Tracking System currently implemented in ALICE. Composed of the Inner (layers 0-2) and Outer (layers 3-6) Barrels, seven layers of ALPIDE [6] detector chips are stacked together on staves for mechanical support. ALPIDEs are MAPS specifically produced for the ALICE experiment by TowerJazz using their 180 nm CMOS imaging process.

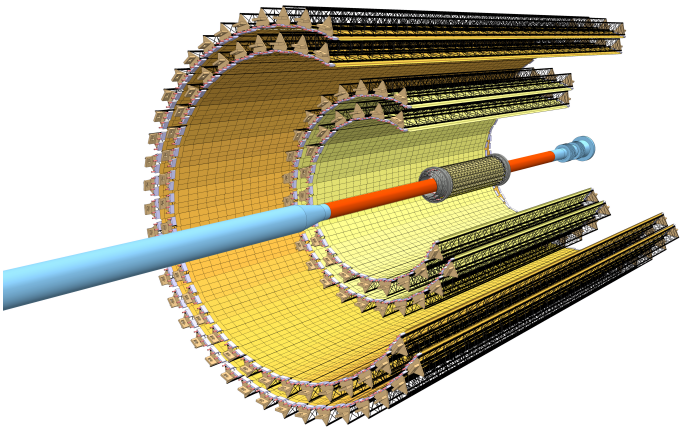

Figure 1.2: Layout of the ITS2. The ALPIDE strips are placed on staves for mechanical support. Image from [6]

During the LHC Long Shutdown 3 (LS3) in 2026-2030, a new Inner Tracking System, ITS3, is set to replace the three inner-most layers of ALICE with new MAPS detectors produced with the TPSCo 65 nm CMOS technology, which facilitates the production of larger wafers, allowing for 300 mm diameter wafers as opposed to the 200 mm diameter wafers produced for ITS2, as well as denser electronic circuitry. One of the most important features of ITS3, which distinguishes it from ITS2, is the **reduced material budget**, arriving at a value of about 0.07 %X_0 per layer whereas the ITS2 currently takes advantage of a material budget of 0.3 %X_0, with each layer set to be comprised of **cylindrical, curved sensors**, thinned down to 50 µm thickness. Carbon foam keeps each layer in place and thus discards the need for mechanical support in the form of staves as well as any circuit board connections. With these wafer cylinders, it is then possible to move the layers closer to the collision point at ALICE, i.e., within 19 mm of it. Thus, with the next generation of MAPS being implemented in ITS3, a highly improved spatial (3.4 µm to 7 µm) and pointing resolutions are expected, as well as better vertex reconstruction, especially for low transverse momentum (about 100 µm at $p_{\mathrm{T}} \sim 100$ MeV) particles, which would be less affected by multiple scattering due to the low material budget [10]. In order to test the 65 nm CMOS technology, the Multi-Layer Reticle 1 (MLR1) [11] submission was developed in order to investigate different manufacturing processes, doping profiles, and circuitry. This submission produced test structures such as the APTS [12] and DPTS [13], of which the APTS was investigated in this work.

To minimize the amount of material from services such as data transmission lines and power distribution within the active area of the detector, the ITS3 design relies on large-area sensors that are interconnected only along their short edges. This is enabled by the implementation of **stitching**, a technique in CMOS manufacturing that allows sensors to exceed the reticle size limit of the lithography process. In stitching, different parts of the circuit are exposed sequentially, such that multiple reticle-sized segments combine seamlessly into a single, larger sensor. To investigate the expected production yields and operational stability of such large-area stitched sensors, prototype devices were produced. Examples of such stitched sensors include the MOSS and its smaller

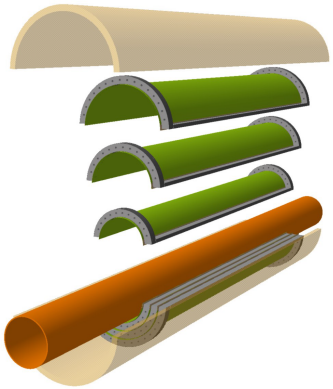

Figure 1.3: Schematic of ITS3, including both half-barrels [10]

prototype, BabyMOSS (Sec. 2.1), which was investigated in this thesis.

1.2.2 ALICE 3

The LHC will be undergoing an upgrade of its own in the current decade during the upcoming LS3 in order to increase the collision rate capabilities five times for proton-proton and heavy ion beams and therefore the integrated luminosity of the accelerator tenfold when compared to the nominal value, rising to 3000 fb^{-1}, opening a new world of possibilities for all types of measurements at the four major experiments, including ALICE. The peak luminosity would then be enhanced to a value of $5 \times 10^{34}\,cm^{-2}s^{-1}$ from $2 \times 10^{34}\,cm^{-2}s^{-1}$. The resulting accelerator is to be named **High Luminosity LHC (HL-LHC)** [14]. With said luminosities, more data can be gathered about for number of rare interactions, which can then be analysed with high statistics.

In order to take advantage of the highly increased interaction rates at the collision points in ALICE, a new detector concept will then be implemented, **ALICE 3** [15],[16], which would then be capable of measuring interactions with a rate of 24 MHz for proton-proton collisions, as well as a rate of around 93 kHz for lead-lead runs.

A *retractable* **vertex detector** is to be fitted inside the beam pipes, starting at 15 mm radially to the nominal interaction vertex as to allow the LHC beam to pass, and closing in to 5 mm at stable beam conditions as to begin data-taking. The vertex detector is set to have a position resolution of about 2.5 µm, fitted with three cylindrical barrels and three discs on either side.

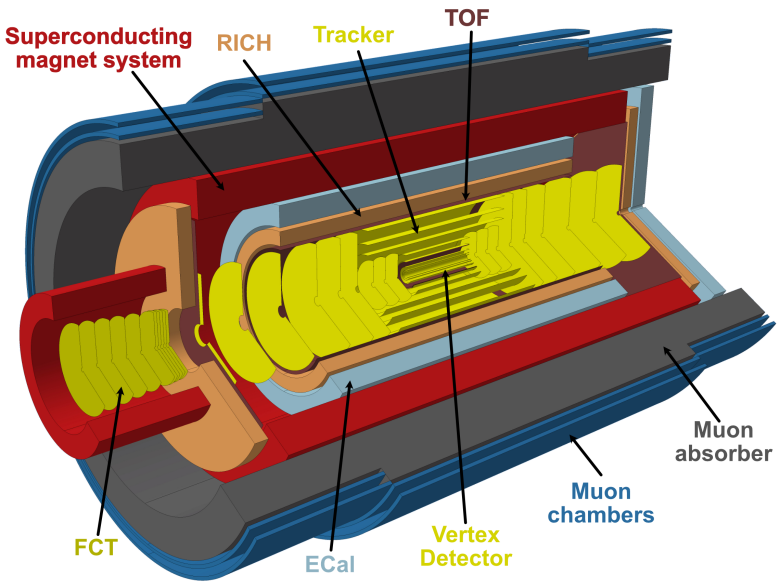

Figure 1.4: The ALICE3 detector concept. An inner vertex detector and outer MAPS tracker with the classic barrel design function in tandem with silicon disks in the forward and backwards directions. PID is performed using an inner and outer time-of-flight detector, RICH detector, forward conversion tracker (FCT) and muon chambers, as well as an electromagnetic calorimeter (ECAL). This version of the detector concept was taken from [15].

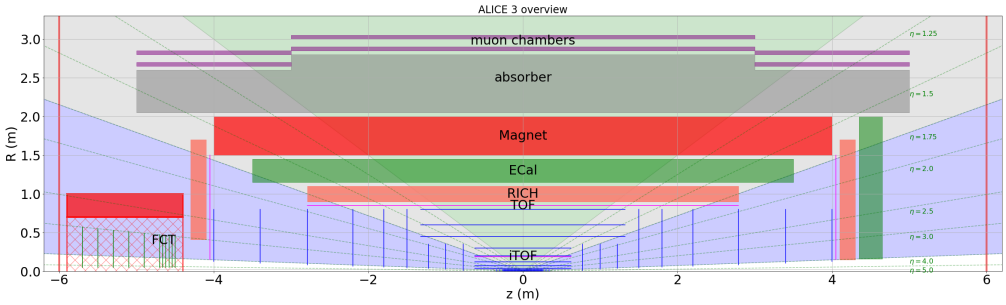

Figure 1.5: Schematic cross-section of the ALICE 3 detector layers [15].

Directly after the vertex detector and the inner barrel layers mentioned above come the **outer tracker** barrels, also based on MAPS technology. They consist of eight cylindrical layers and nine discs on each side of the interaction point, covering a large active area of several square meters, with an aimed spatial resolution of 10 µm. The large detector area has a direct impact on the pixel design: to maintain reasonable readout speed and power consumption while ensuring high granularity, the pixels must balance size, signal-to-noise ratio, and integration of readout electronics. Apart from this, as can be observed in Fig. 1.5, multiple PID detectors are also present, including both inner and outer time-of-flight (TOF) detectors, a Ring Imaging Cherenkov (RICH) detector, and the Forward Conversion Tracker (FCT), which is specifically designed to measure photons, even at low transverse momenta (down to $\sim 2\,\mathrm{MeV}/c$). This is

achieved by directly detecting dielectron pairs converted from said photons [15, 16].

Due to the discs on either side of the interaction point, larger pseudorapidity ($|\eta| < 4$) ranges are able to be investigated, again improving the probability of measuring particles with small outgoing angles and therefore having a much better angular resolution. In the current ALICE experiment, the TPC is used in tracking in collaboration with the ITS2, while in ALICE 3, the TPC would be removed, and tracking would be done purely through the MAPS trackers installed at the heart of the detector, with a reduced readout time in order to remain on par with the interaction rate at HL-LHC. The ITS3 prototypes are therefore also prototypes for the ALICE 3 outer tracker, since the ALICE 3 MAPS tracker will be based on similar sensor technology as the current ITS3 prototypes.

2 Experimental Setup and Procedure

2.1 BabyMOSS

The **MO**nolithic **S**titched **S**ensor is a proof-of-concept prototype wafer-scale sensor produced with the main goal of testing the stitching technology described in Sec. 1.2.1 for yield. Yield is defined as the number of sensors considered fully functional (successfully passing all required operational tests) divided by the total number of sensors produced [17]. Repeating Sensor Units (RSUs) are stitched together to build a sensor with a larger active area. Ten RSUs are stitched together, as can be seen in Fig. 2.2, to create a single MOSS sensor with a length of 25.9 cm.

One BabyMOSS prototype contains one RSU, while integrating the left and right end-caps, is divided into two half-units, top and bottom, each with four regions. Each region of the top half-unit comprises 256 row $\times$ 256 column pixels, each with a size of 22.5 $\times$22.5 µm^2, whereas the bottom half-unit has 320 $\times$ 320 pixels with a size of 18 $\times$ 18 µm^2 each. The difference in pixel pitch is helpful for yield comparison and general sensor characterisation, as more pixels on the same area give the sensor more possibilities to be defective. In addition, different implementations in upper and bottom half-units may provide insight into differences in behaviour.

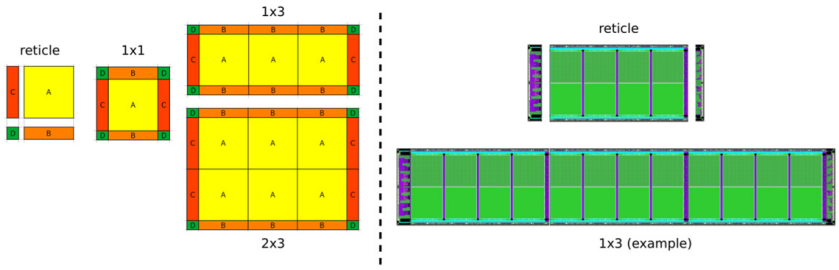

Figure 2.1: On the left: generic stitched objects, outlining the general methodology. On the right: one MOSS reticle (BabyMOSS) and a stitched sensor with RSUs [18].

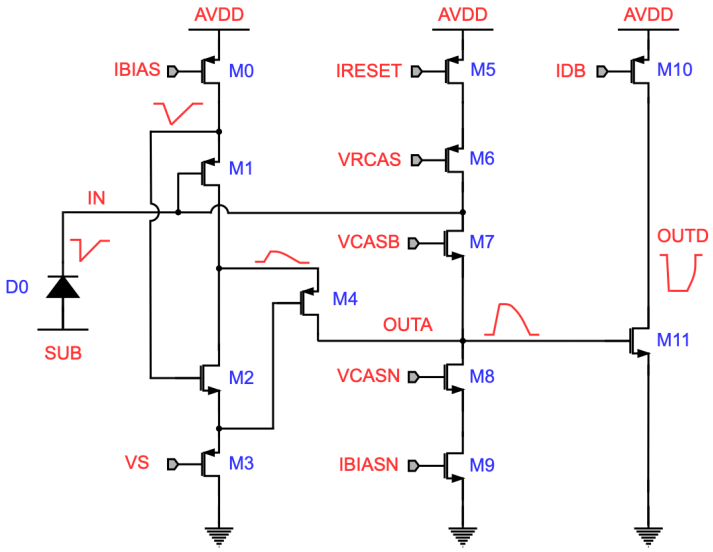

Figure 2.3: Front-end circuitry of the MOSS. Crucial current and voltage inputs can be seen on the schematic [19].

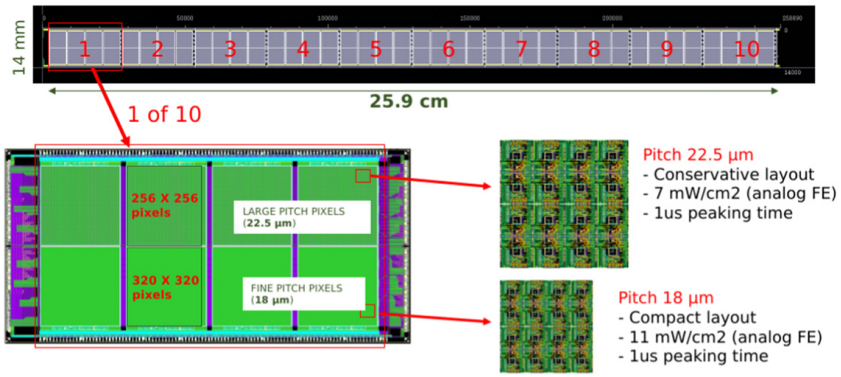

Figure 2.2: A full stitched MOSS with 10 RSUs (BabyMOSS). The top and bottom halves of an RSU have different pixel pitches and numbers of pixels. [18].

Each of the regions also possesses different properties depending on the individual layout, as can be seen in Table 2.1, affecting performance in yield, which is to be investigated. In Fig. 2.3, the different voltage and current control inputs can be found. VCASB is, for this work, the most important control input, as any changes in this voltage have a direct and inverse effect on the mean threshold in any given region, i.e., thresholds are lower for higher VCASB values. In Fig. 2.2, one can observe how the stitching technique produces larger units, specifically how the active area directly increases when removing and replacing the outer units (end-caps), as is also the case with the MOSS.

	Region 0	Region 1	Region 2	Region 3
TOP	Standard	Larger input transistor (M1)	Larger discriminator input transistor (M11)	Larger common-source transistor (M2)
BOTTOM	Standard	Standard	Standard	Slightly different layout

Table 2.1: Differences in the region front-end circuitry [19].

2.2 APTS

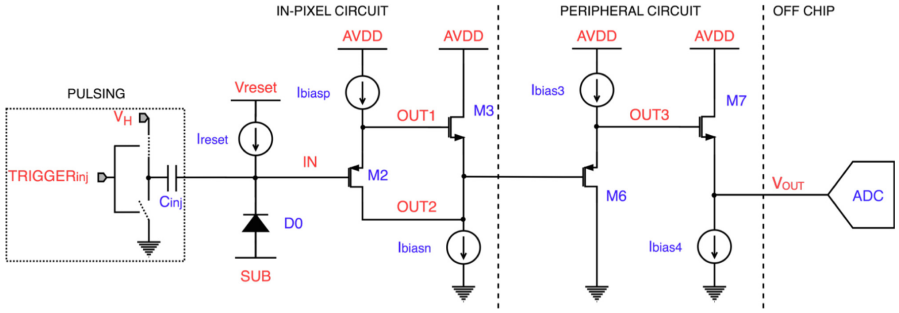

Figure 2.4: Front-end circuitry of the APTS [12].

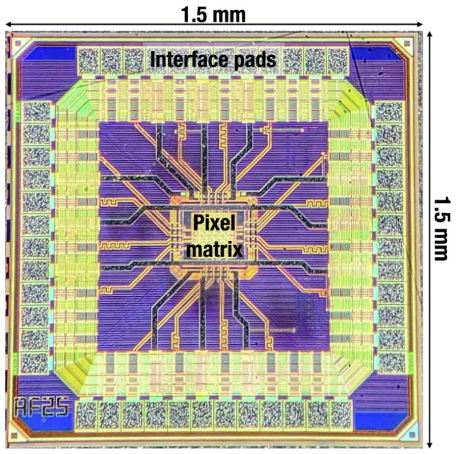

Figure 2.5: A close-up of the APTS chip [12].

The pixels for the Outer tracker (OT) are generally designed with a larger pitch to reduce readout complexity and power consumption. However, it is not yet clear whether charge collection remains effective for such large pixels after irradiation, due to potential losses along the long drift distances from the corners and edges. To address this, prototype large-pitch sensors are being produced. In this thesis, as these sensors

are not yet available, investigations are conducted using 25, µm pixel pitch APTS prototypes produced in the MLR1 production for ITS3, with the aim of establishing a systematic methodology for their characterisation. APTS stands for **A**nalog **P**ixel **T**est **S**tructure. The main goal of the APTS characterisation is to document a robust procedure that can be applied in future studies of large-pitch MAPS intended for the proposed ALICE 3 detector (Sec. 1.2.2).

As with the MOSS, the APTS is a prototype pixel structure designed with 65 nm CMOS technology specifically to investigate the **direct analogue readout** of the new MAPS sensors planned to be used for the ITS3. It measures 1.5 mm × 1.5 mm, with a 4 × 4 pixel matrix at its centre. In order to diminish distortion effects caused by the electric field produced by the potential difference applied to the chip , a ring of dummy pixels is also placed around the inner matrix [12]. Manufactured with multiple different pixel pitches, 10, 15, 20, and 25 µm, there were also pixel design differences throughout the different APTS, as can be seen in Fig. 2.6.

The **standard** design is similar to the one used in ALPIDE; a balloon-shaped depletion zone is not wide enough to reach the pixel edges, resulting in relatively slow charge collection almost exclusively through diffusion, with the circuitry placed in a p-well, not directly in the epitaxial layer, to prevent charge collection. The **modified** design implements a deep low-dose n-type implant under the full area, also called a blanket implant. This creates a depletion region covering the full area of the pixel when back bias is introduced, ensuring collection of the charge carriers by drift. The **modified-with-gap** design integrates a gap of 2.5 µm at the edges of the pixel, reducing charge sharing between neighbouring pixels, while increasing the electric field from the depletion region in the lateral direction [12].

The need for sensor variants in the ITS3 design arises from limitations of the 65 nm TPSCo process, which only supports an epitaxial layer thickness of 10, µm, compared to the 25, µm thickness available in the 180 nm process used for ALPIDE. A thinner active layer reduces charge collection, and applying the same standard process would not achieve the efficiency observed with the thicker epitaxial layer. Studies with angled tracks have shown that increasing the epitaxial thickness significantly improves efficiency, highlighting the need for alternative strategies to maintain comparable performance. Consequently, the pixel and process design was optimized to enhance charge collection in the thinner TPSCo 65 nm ISC sensors, building upon the optimization principles developed for the 180 nm TowerJazz imaging technology [12, 20].

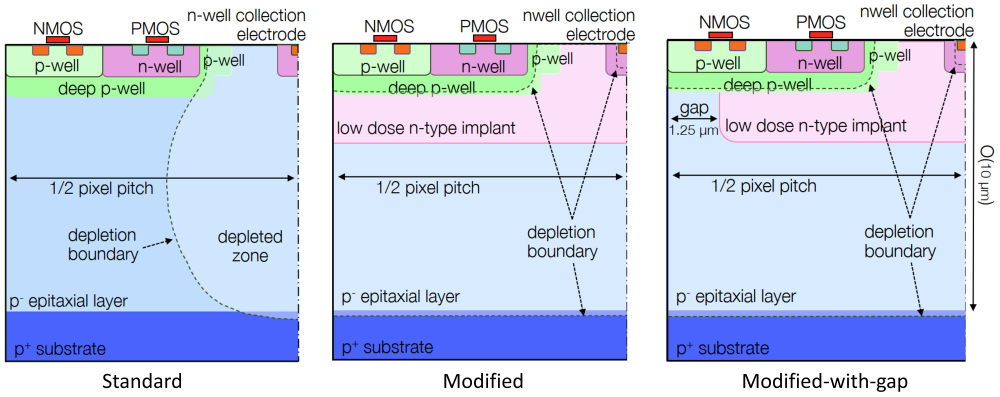

Figure 2.6: Different types of MAPS semiconductor pixel design. The most relevant use in this thesis is "modified with gap". Taken from [21]

2.3 Measurements

This thesis focuses on two main experimental measurements: Laboratory Measurements of the BabyMOSS threshold and fake hit rate trends, and those taken in a one-week period from the 22nd to the 29th of April 2025 at the DESY (Deutsches Elektronen-Synchrotron) accelerator facilities in Hamburg, Germany. Both were taken with similar setups of a beam telescope, with the addition of measurements for the APTS with DPTS and BabyMOSS triggering at DESY.

2.3.1 Laboratory Measurements

For the laboratory measurements, two main properties of the chips were investigated: the (mean) **threshold** and the **fake hit rate** (FHR). The threshold of a given pixel characterises the amount of charge needed for it to register a particle as a "hit". FHR is the number of false hits registered on a pixel when there are no particles passing through. If the threshold is low, a higher FHR is expected to be registered, as there are more noise signals that are then able to surpass the threshold limit and be counted as hits.

Learning about the mean threshold of each region at a given VCASB value, when combining the information with that of the corresponding FHR, allows one to determine optimal functioning parameters of the sensors, for example, for the test beam at DESY in this work. To this end, threshold and FHR scans were performed in the laboratory on multiple BabyMOSS in the test beam telescope setup.

Threshold Scan

A BabyMOSS incorporates a pulsing functionality that enables the injection of a defined amount of charge into the analogue input stage of each pixel individually. Each pixel's internal capacitor collects charge for a given VCASB, then injects said charge into the collection diode, mimicking the charge deposition process of a real ionising particle. The measured probability, i.e. how many injections are considered hits over the total

number of injections considered a hit, is then plotted in an **S-curve** against the amount of charge injected. The point at which 50% of the injections are considered hits is taken to be the **threshold**, i.e., the minimum amount of charge a particle must deposit in order to be registered as a hit. The fit parameter, the slope, of the S-curve is then taken to be the noise. These thresholds can be graphed in a histogram across all pixels under the same conditions (for the BabyMOSS, one of the 8 regions) and fitted with a Gaussian function to then find the mean value of the threshold. Examples for an S-curve and a threshold distribution can be seen in Fig. 2.7a

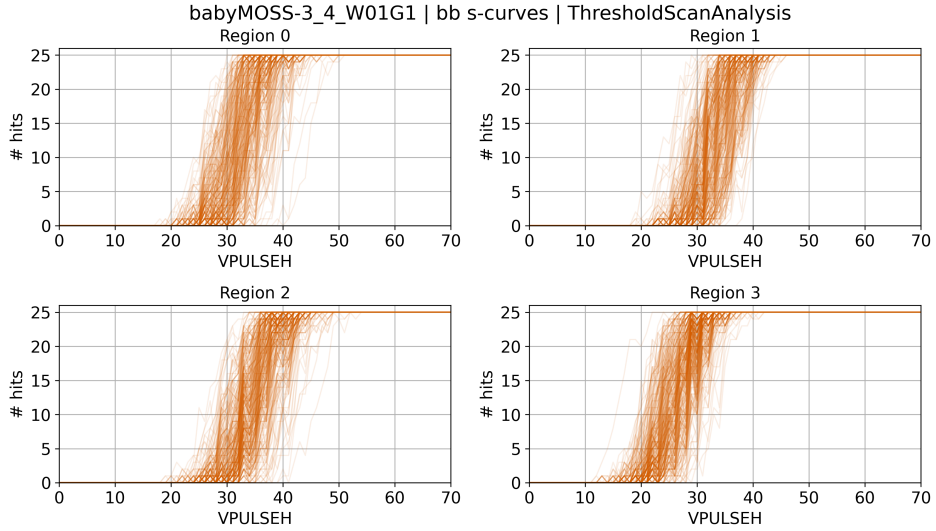

(a) Examples for S-curves on a BabyMOSS bottom half-unit.

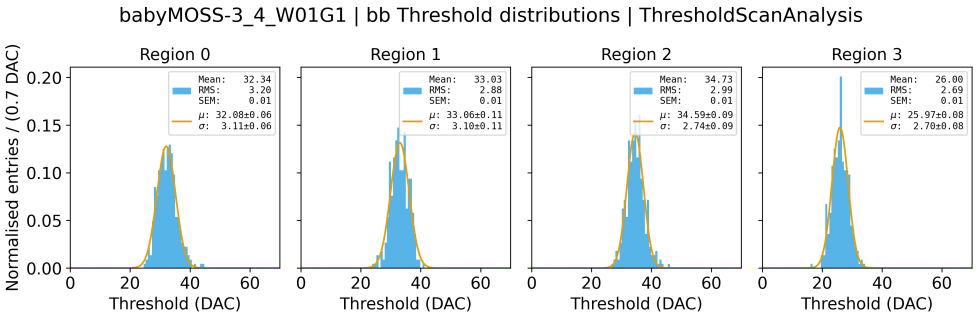

(b) Examples of threshold distributions on a BabyMOSS bottom half-unit.

Figure 2.7

FHR Scan

A **fake hit** is a hit readout output from a pixel indicating that a particle has passed through it when there are none present (i.e., not in a particle beam situation). For a preset number of events, the FHR of each region is calculated by dividing the number of fake hits by the total density of events, as in Eq. 2.1.

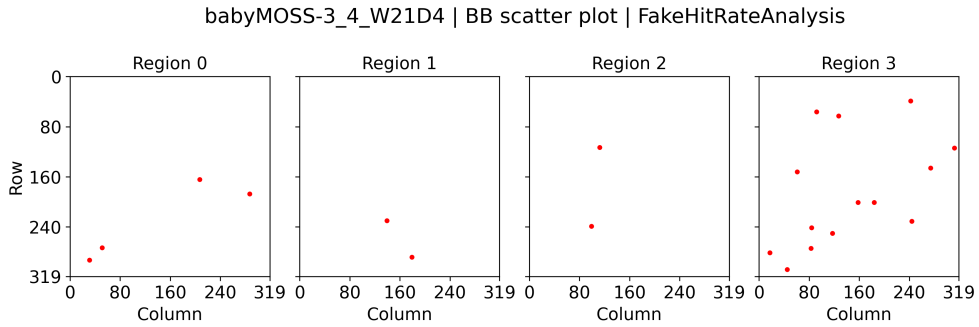

Figure 2.8: An example of an FHR scatter plot visualising which pixels registered hits, although there is no particle beam passing through it.

$$\mathrm{FHR}_{\mathrm{reg}} = \frac{\text{No. of fake hits}}{\text{No. of predefined events} \times \text{No. of pixels in region}}. \tag{2.1}$$

Analysis Development

In order to automate the threshold and FHR scans, a Python script optimised to simplify the analysis process was developed.

Firstly, the threshold and FHR scan analysis programs provided by the ALICE Collaboration were chained together, and the results were grouped according to chip and VCASB value. Using this information, it was then possible to create multiple comparative plots of different thresholds across different regions and different chips, including comparisons of threshold means across regions, threshold distributions and FHRs.

One of the types of figures produced was a FHR map of all eight regions on **all** BabyMOSS layers for a given VCASB value, which was planned to be used at the test beam at DESY described in Sec. 2.3.2 as a means of initial alignment. One example of this figure can be seen in Fig. 2.9a.

Chip	**Sensor identifier**
Chip 1	babyMOSS-2_3_W01G1
Chip 2	babyMOSS-2_4_W01G1
Chip 3	babyMOSS-3_2_W01G1
Chip 4	babyMOSS-3_4_W01G1
Chip 5	babyMOSS-3_4_W21D4

Table 2.2: Mapping of chip numbers from Fig. 2.9(a) to BabyMOSS sensor identifiers.

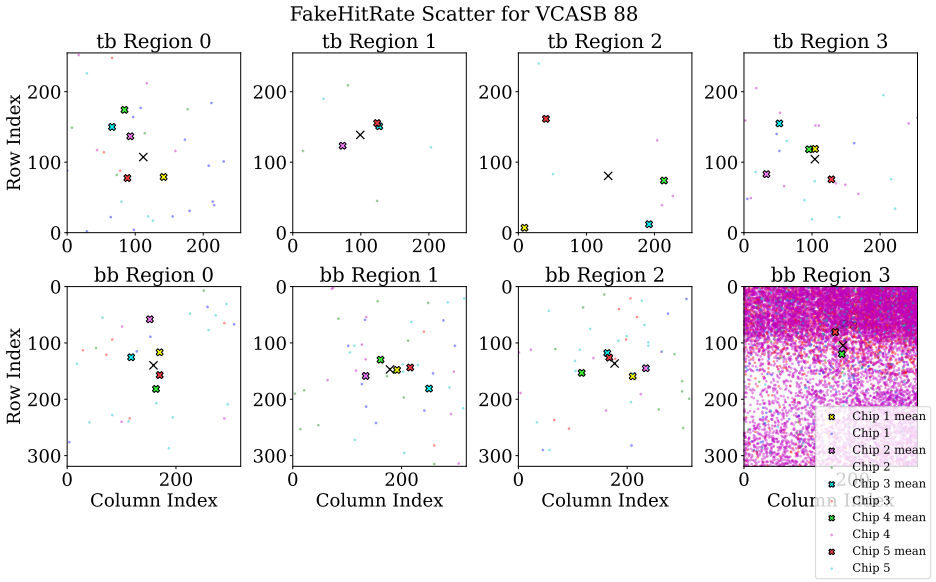

(a) FHR scatter overlay. At this VCASB, one can see the extreme increase in fake hits on the bottom half-unit region three due to the low threshold.

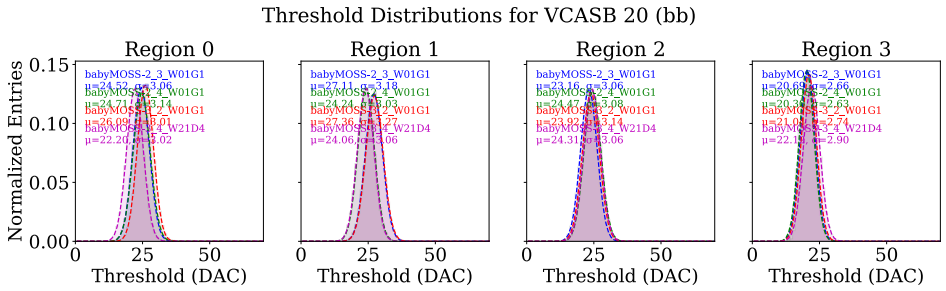

(b) An example of the threshold distribution overlay for bottom half-unit regions, comparing different BabyMOSS mean region thresholds at a given VCASB value. This information helps determine the correct operational parameters.

Figure 2.9

Beam Telescope

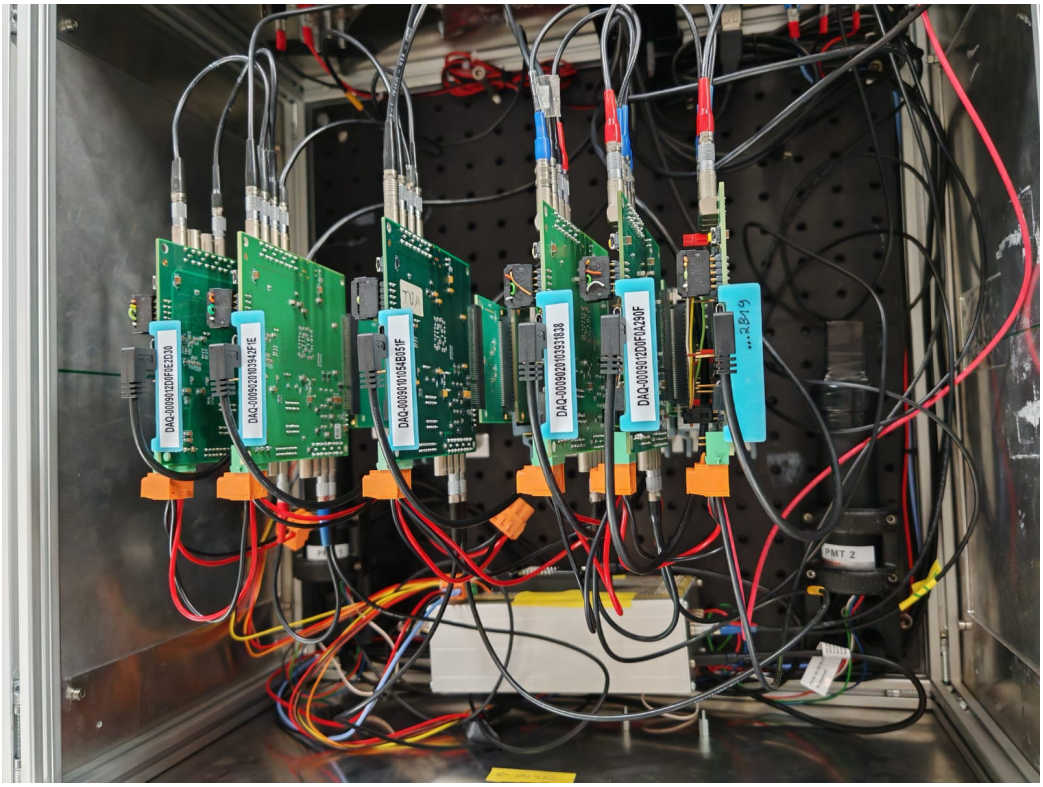

Figure 2.10: The telescope setup for the rotating BabyMOSS measurements. The DUT-DAQ setup is in the middle layer, standing on the rotating stage. The DAQ board outputs and inputs can be seen on the sides of each board. A triggerboard is used for triggering, in conjunction with two photomultipliers with scintillators in the up- and downstream directions of the beam.

The telescope consists of a stainless steel box fitted with an optical breadboard, on which the aluminium boxes containing the chips, as in Fig. 2.11, as well as the readout cards, are placed and attached with M6 screws. The layers of BabyMOSS chips connected with adapter Printed Circuit Boards (PCBs), so-called Raiser Cards, to their corresponding DAQ boards were placed at a spacing of 25 mm from each other as in the following schematic. The BabyMOSS chip ID's, their position, back bias voltage values (V_{BB}), as well as the corresponding DAQ boards used can be found in Table 2.3.

(a) (b)

Figure 2.11: The aluminium holders for the BabyMOSS chips, **(a)** covered as in the telescope, **(b)** showing the full proximity card, which the BabyMOSS is bonded to.

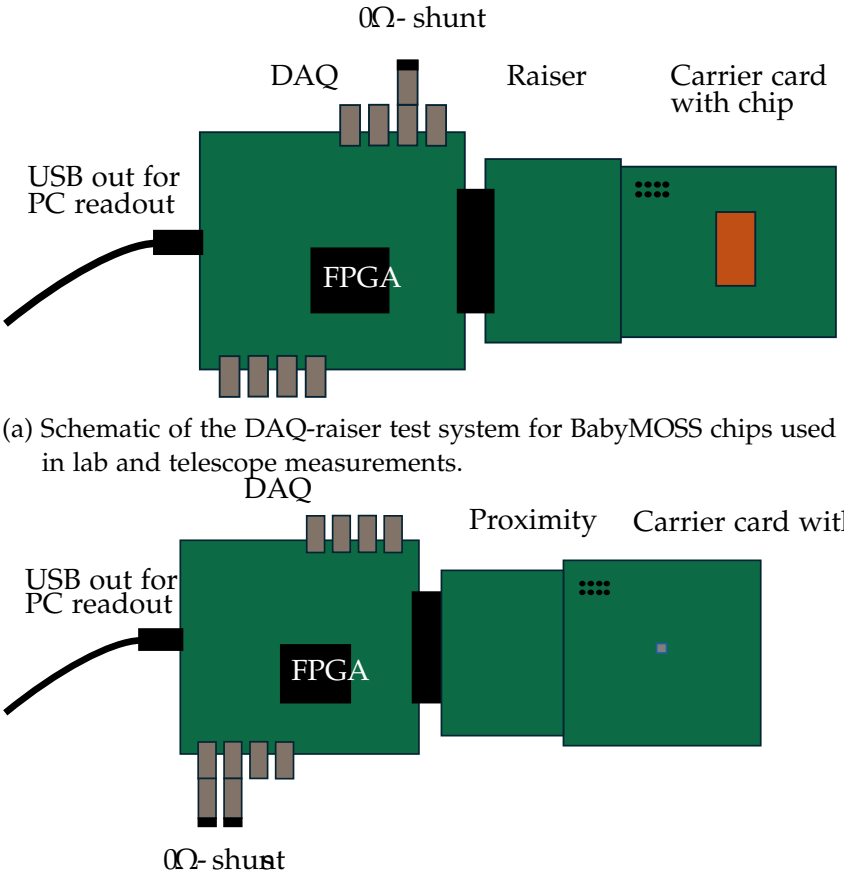

(a) Schematic of the DAQ-raiser test system for BabyMOSS chips used in lab and telescope measurements.

(b) Schematic of the DAQ-raiser test system for APTS chips used in lab and telescope measurements. The same test system was used for DPTS measurements.

Figure 2.12: Overview of the DAQ-raiser test setup for MAPS chips. Subfigure (a) shows the laboratory and telescope configuration; subfigure (b) shows an additional view or related schematic.

The general setup for all measurements taken with the BabyMOSS can be seen in Fig. 2.12. A Data Acquisition (DAQ) board is connected through a raiser board interface to the carrier card holding the BabyMOSS chip. The DAQ board contains an FPGA to facilitate readout control of the sensor.

In order to allow angled measurements with the BabyMOSS (with respect to the beam), an optical rotating stage on a rail was installed at the spacing of the DUT chip, babymoss_3_4_W01G1.

2.3.2 DESY Testbeam

The telescope setup was taken to DESY and placed in a beam of 2.4 GeV electrons at test beam area 22, behind another telescope setup. After initial laser alignment, there was a trial to utilise the FHR map on all regions of a BabyMOSS for more exact alignment using the beam. Unfortunately, this method resulted in being too difficult to use as the number of events being read out on each of the layers created a very dense hitmap,

Sensor	DAQ board	Z-position [mm]	V_{BB} in V
3_4_W01G1	DAQ-0009012D0F0E2D30	0	-1.2
2_4_W01G1	DAQ-0009020103942F1E	25	-1.2
3_4_W21D1	DAQ-00090101054B051F	100	-1.2
2_3_W01G1	DAQ-0009020103931838	175	-1.2
3_2_W01G1	DAQ-0009012D0F0A290F	200	-1.2
1_2_W01G1	DAQ-0009020103942B19	225	0

Table 2.3: This table contains the BabyMOSS units used, their positions in beam direction (Z-axis), the back bias voltages set on each of them and the DAQ-board identifiers corresponding to those used at the test beam.

as shown in Fig.2.9, which hindered any kind of visual confirmation of good or bad alignment. The reason is suspected to be the projection of all six BabyMOSS layers on one hitmap, with too many events to distinguish properly.

Initial manual alignment was performed with help of a laser in the test beam area. Revising alignment by examining FHR "scans" and not being able to move any chip in the setup except manually resulted in the deactivation of the electron beam multiple times, disrupting data-taking. One possible improvement to the setup could then be [a remote-controlled motor stage in the x-y plane, facilitating changes in the chip positions with less time investment.] After solving some hardware-related readout and data-taking issues, readout of the test-beam events was possible using the EUDAQ2 software.

EUDAQ2 is a data acquisition software originally developed for the EUDET and EUDET-type pixel detector telescopes [22]. An integrated GUI acts as the control method for the readout, showing the number of events read out, how many are still to be read out, event rate and trigger rate, allowing for swift and concise comparison of the readout to the expected readout, dependent on the particle type, momentum, and count in the beam.

BabyMOSS Measurements

At first, a flat configuration was used to take data, where the DUT had its plane perpendicular to the beam direction. The DUT was also rotated to angles of 15°, 30°, 45°, and finally 60° with respect to the beam direction. The goal was to investigate any changes in the spatial resolution and efficiency due to the changes in the effective volume of each pixel in which the ionising particle traverses, as such depositing more energy.

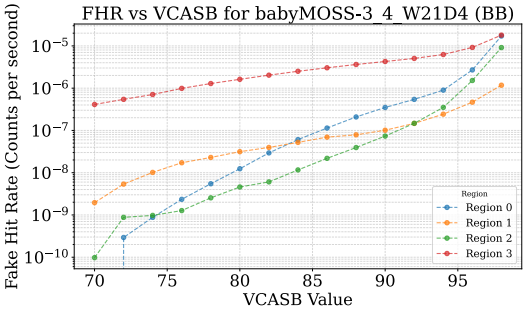

(a) Fake Hit rate on the bottom half-unit of the DUT.

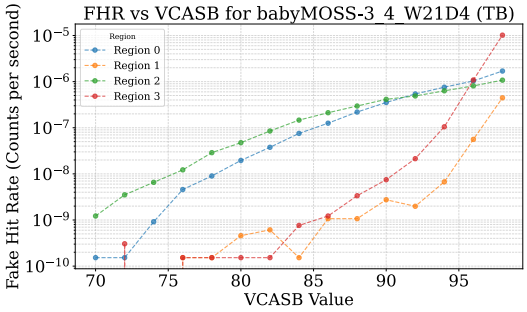

(b) Fake Hit rate on the top half-unit of the DUT.

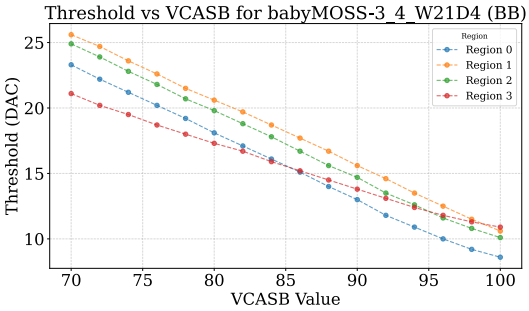

(c) Mean threshold on the bottom half-unit of the DUT.

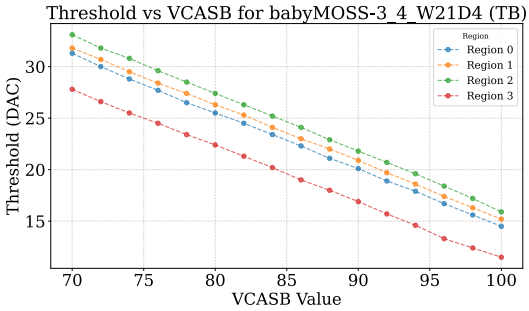

(d) Mean threshold on the top half-unit of the DUT.

Figure 2.13: Threshold means and fake hit rates on the DUT against their corresponding VCASB values.

Since no threshold scans were done in any of the configurations, lab measurements were used to assign mean thresholds of each region, dependent on the VCASB value applied to the chips at the flat test beam configuration, to which the corresponding values are to be seen in Fig. 2.13. An example of an angled configuration can be seen in 2.14.

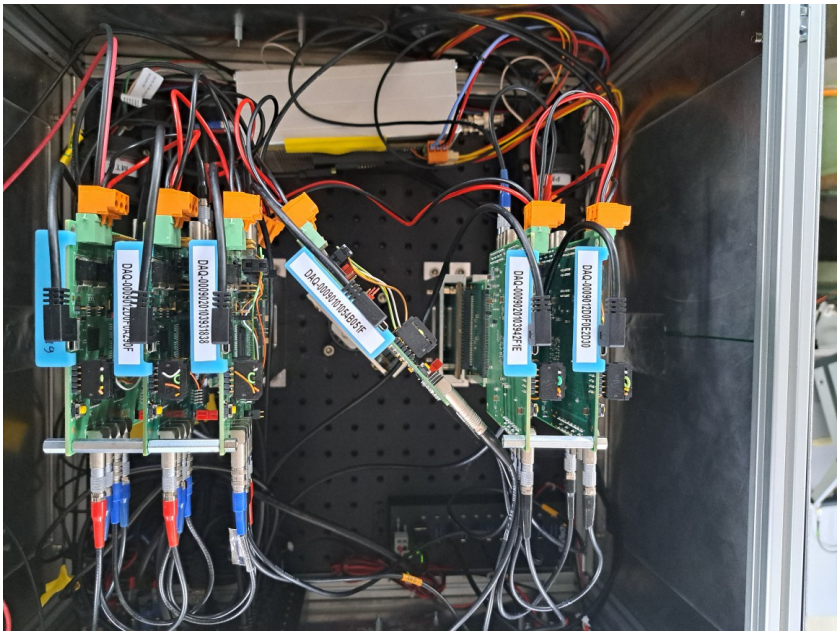

Figure 2.14: The BabyMOSS telescope setup with the DUT at 45° with respect to the beam direction.

APTS Measurements

The rail and rotating stage were replaced with another aluminium box similar to the ones holding the BabyMOSS units, but with an additional DPTS chip layer attached to the APTS layer by two 10 mm screws instead, ensuring parallel DPTS and APTS layers.

The DPTS, **D**igital **P**ixel **T**est **S**tructure, is a sensor produced similar to the APTS with 32×32 rows and columns, with a pixel pitch of 15 µm, developed alongside the APTS [13].

The DPTS is used for triggering on the BabyMOSS as a way to reduce unnecessary hits, as the APTS has a much smaller surface area than the BabyMOSS, therefore increasing readout efficiency by effectively ignoring most events outside of the DPTS area, focusing on the particles actually hitting the DPTS and therefore APTS.

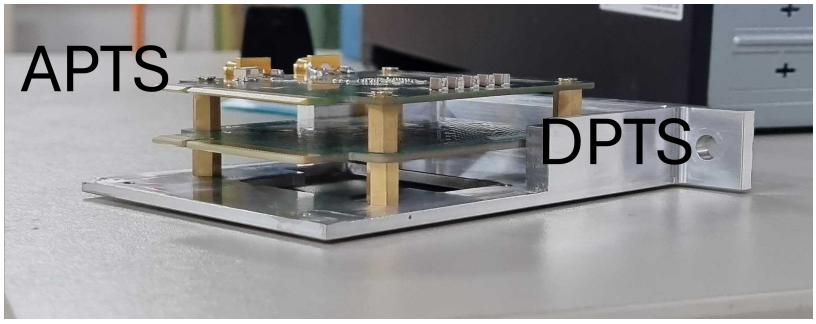

Figure 2.15: The APTS and DPTS cards screwed together

At first, the chip APTS_AF25P_W22T06 was installed in the telescope with no

back-bias voltage. It was then replaced with APTS_AF25P_W22T07 to continue measurements at no back bias, $-1.2\,\mathrm{V}$ as well as $-2.4\,\mathrm{V}$. Unfortunately, it was soon clear through looking at the output from the analysis framework Corryvreckan (Sec. 3.1.1) on-site that the pixel (***3***, ***2***) on the APTS_AF25P_W22T06 pixel matrix was non-functioning. Due to the small number of pixels in general, and to the fact that there are no pixels outside of the outer four pixels, resulting in reduced charge sharing in the edge regions, only the inner four are able to be taken into account during analysis, as without charge sharing, tracking becomes much less accurate. Measurements continued with this setup.

3 Analysis

3.1 Methodology

3.1.1 Corryvreckan Framework

Corryvreckan [23] is a test beam data analysis and reconstruction framework. With integrated modularity, users are able to add to the framework without needing to modify its core capabilities. During and after the test beam at DESY investigated in this thesis, Corryvreckan was used for all analysis. Corryvreckan is based on ROOT.

In order to use Corryvreckan, the output from the EUDAQ2 readout system is used along with configuration files detailing which modules are to be used to reconstruct particle positions on layers based on cluster positions, fit tracks, align the telescope and calculate efficiencies, as well as the initial physical geometry of the telescope. This defines the distances between all layers, any masked pixels, the material budget of every layer and any physical displacement in rotational and translational degrees of freedom. This geometry also includes the pixel size. Every alignment step produces a new geometry, only changing the translational and rotational position of any given layer, depending on the method used. One reference layer must be defined in order to calculate displacements around it. This layer should not be the DUT so as not to skew the results produced.

For this thesis, the following procedure was put in place for alignment and subsequent analysis:

1. **Masking**: A masking module was used to mask all pixels exceeding hit frequency higher than twenty times the mean number of hits on all pixels, which may not have existed in the initial masking file. These are considered noisy pixels and are therefore not considered for further alignment or analysis.

2. **Prealignment**: An initial translational alignment is executed by calculating the distribution of distances between each cluster in each layer to the corresponding one on the reference layer. A fitting method is then applied to the distribution, and a shift is applied according to the parameters calculated. In this work, the mean of a Gaussian fit was used for BabyMOSS prealignment, and the maximum value of the distribution was used for the APTS. A clustering module is used here.

3. **Telescope Alignment**: The reference layers of the telescope, i.e., all layers except the DUT, are aligned using one of many algorithms. To this end, a tracking algorithm is first applied to the clusters found by the clustering algorithm. In this work, telescope tracking was always executed using the Straight-Line method.

Telescope alignment was repeated twice, with the second time having a tighter spatial cut on the tracking, refining the subsequent geometry.

4. **DUT Alignment**: This step was repeated three times, again with smaller and smaller spatial cuts, forcing good track quality while aligning only the DUT and *not* the telescope layers. A different alignment algorithm module is utilized, specifically for DUT alignment.

5. **Analysis**: This is the final stage of the pipeline and the one where efficiencies are calculated using specific Analysis modules, as well as residuals on the DUT. None of the layers in the telescope is further aligned during this procedure.

All configuration files used are to be found in

Tracking

In order to set any path that a particle took in a given setup, a track, the approximate positions of the particles on each detector layer must be calculated or measured. To this end, **charge clusters** are defined. A cluster can be defined at will, but is usually, as in this case, a group of pixels neighbouring each other which have registered hits at similar times. Each of these clusters is assigned a centre defining the cluster position.

It is to be noted that a **pixel** is in itself defined through a hit/no hit, as well as position in row and column coordinates of the detector.

A **track** is a collection of clusters, with track positions at each layer, subsequently defining the path a particle took through the telescope. To find these tracks, they must first be fitted using an algorithm, of which there are three integrated in Corryvreckan, each integrating hit uncertainties and multiple scattering differently.

The **Straight-Line** method does not take multiple scattering into account, only considering hit position uncertainties. **General Broken Lines** (GBL) [24] includes scattering uncertainties in its algorithm, matching the kink expectations with the actual measurements to create a non-straight path depending on material budget and particle momentum. The **Multiplet** method creates two "tracklets" by dividing the reference system into two and applying either of the two methods already mentioned, joining them at a user-predetermined point in the beam direction (z), usually the DUT. The former two methods were used in this thesis.

To quantify track quality, the χ^2 of tracks found is calculated depending on the tracking method and plotted with the number of tracks against it. The distribution of $\frac{\chi^2}{\text{\# of degrees of freedom}}$ of a well-aligned telescope can be seen in Fig. 3.1. A clear shift of the mean towards one implies good alignment as it indicates a minimisation of the χ^2 function, i.e. the nearing of expected values of positions from the cluster centres to the fitted residuals (see below) [25].

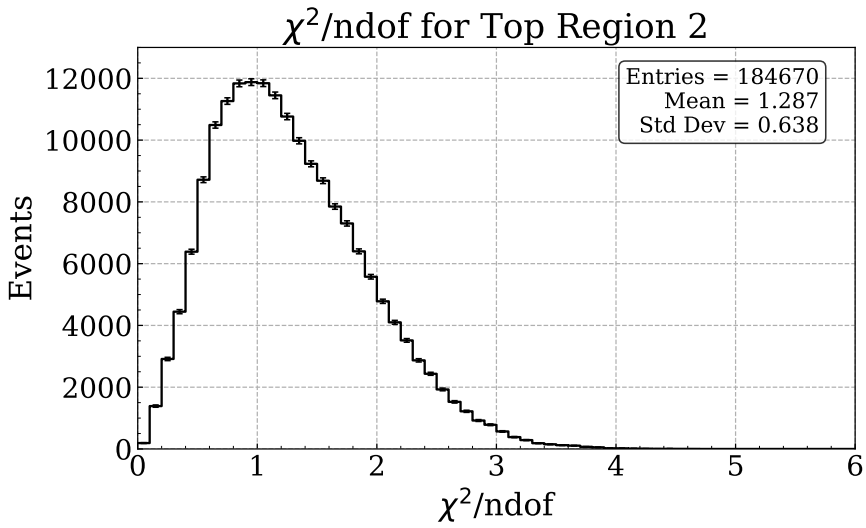

Figure 3.1: An example of the χ^2/ndof distribution for a well aligned detector. The mean close to one and a longer, asymmetric tail indicate good alignment.

Residuals

The residual of an event is defined as

$$\text{res} = x_{track} - x_{cluster}, \tag{3.1}$$

i.e. the distance between the position of the fitted track and the center of the cluster corresponding to it on a given sensor layer. The shape of distribution of the number of events against the residual value is an important sign of **(a)** good alignment and **(b)** the spatial resolution of the sensor. An example of a such a distribution of a well-aligned sensor can be found in Fig. 3.6.

3.1.2 Spatial Resolution

The spatial resolution of a detector quantifies how precise it can measure a particle hit's position. As such, it can be crudely evaluated simply from the geometry of the pixel. Seeing as pixels are square, one would find the resolution as the root mean square of a square distribution along the length of a pixel in one axis in the detector plane. This is equivalent to a spatial resolution of

$$\text{RMS} = \sqrt{\frac{1}{\text{pitch}} \int_{-\frac{\text{pitch}}{2}}^{\frac{\text{pitch}}{2}} x^2 dx} = \frac{\text{pixel pitch}}{\sqrt{12}} \tag{3.2}$$

in a given direction.

Of course, a square distribution is not a perfect description of a pixel, as there are other factors affecting the probabilities of hits on the pixel, such as charge sharing with neighbouring pixels. Statistically, this smoothing of the edges of the distribution is reflected in the residual distribution of a sensor. From the standard deviation of this

distribution, along with the tracking resolution, it is possible to calculate the effective spatial resolution of a pixel detector using

$$\sigma_{spatial} = \sqrt{\sigma_{res}^2 - \sigma_{track}^2}. \tag{3.3}$$

Eq. 3.3 can be interpreted as the standard deviation of the distances between measured and real positions of the particles on the detector, being derived from the convolution of the the uncertainties from the spatial resolution and to find the width of the residual distribution, more precisely $\sigma_{res}^2 = \sigma_{spatial}^2 + \sigma_{track}^2$.

As previously discussed in Sec. 1.2.2, ALICE3 is expected to have a spatial resolution of about 10 µm in the outer tracker layers, whereas ITS3 is set to have intrinsic resolutions ranging from 3.4 µm to 7 µm [10].

Alignment

As outlined in Sec. 3.1.1, multiple alignment algorithms are available in Corryvreckan [23], varying in functionality. For the telescope alignment, `AlignmentMillipede` was used successfully, while `AlignmentDUT` was utilized for the DUT. Alignment algorithms all operate similarly, minimizing the **width** of the residual distribution and centering it around zero, which is influenced by the material budget (multiple scattering), distances between the layers, tracking uncertainty (initial geometrical spatial resolution) and beam energy. All alignment modules then edit and produce a new geometry, where for telescope alignment, the translational degrees of freedom in the plane perpendicular to the beam direction were allowed, as well as all rotational alignment. For DUT Alignment, X and Y translational alignment, and all rotational alignment were implemented [23].

As has been mentioned in Sec. 3.1.1, the beam momentum is an essential factor of any tracking algorithm, specifically GBL. After running simulations with Geant4 [26], a beam momentum of 2.1 GeV/c was found to be more reasonable due to the parasitic nature of the telescope position, rather than 2.4 GeV/c. This beam momentum was used for all further alignment and analysis.

3.2 BabyMOSS Results

This section discusses the results from analyzing the BabyMOSS and APTS data using the Corryvreckan framework.

For the BabyMOSS, each region in the eight-region matrix of the sensor was individually aligned and analysed in order to minimize discrepancies in the efficiency calculations, as well as the fact that Corryvreckan was developed with detector with only one particular sensor area in mind. Furthermore, as outlined in Sec. 2.1, the slight differences in region layout and circuitry call for individual evaluation in order to be able to compare performance. For the angled measurements, the telescope region on which most of the angled geometry is projected was used for alignment, e.g. when analysing the third top region on the DUT, the second top region was employed for the larger DUT angles.

3.2.1 Detection Efficiency

The detection efficiency of a sensor is defined as

$$\text{Efficiency} = \frac{\text{\# of associated clusters corresponding to valid tracks}}{\text{total \# of valid tracks intersecting the sensor}}. \tag{3.4}$$

The efficiency quantifies how well the sensor can measure all particles passing through it. For track reconstruction, the detection efficiency affects how accurately a particle path can be reconstructed, as missing hits on a sensor due to low efficiency skew the uncertainty of which paths a particle may or may not have taken. As such, a high detection efficiency ensures that all interactions are properly recorded and minimal information is lost.

Threshold Dependency

As discussed in Sec. 2.1, the threshold of a given pixel, or on average across the whole sensor, is highly dependent on the voltage variable input VCASB. Multiple different VCASBs were applied on the BabyMOSS DUT in the laboratory, and threshold scans were conducted to find the corresponding mean threshold for each region. A similar procedure was then used in the test beam at DESY, and the results were cross-referenced to the laboratory results in order to see the dependency of the efficiency on the threshold values. The raw VCASB measurements can be observed in Fig. **??**. All these measurements were taken with the DUT perpendicular to the incoming beam.

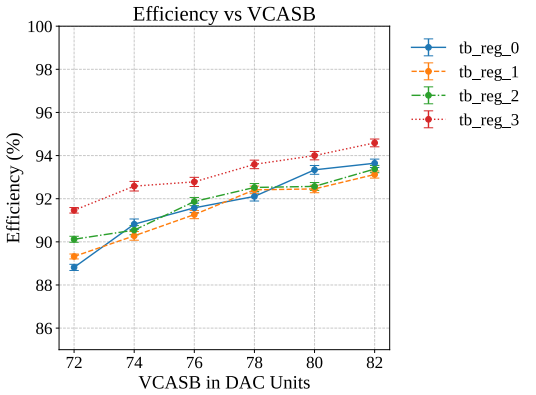

(a) Mean efficiency on each top BabyMOSS region against VCASB. An evident trend of lower efficiency against lower VCASB is observed.

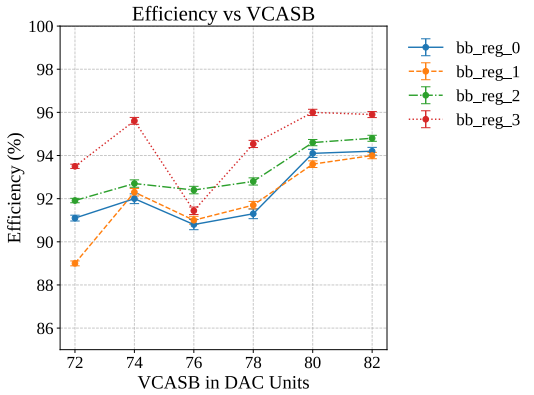

(b) Mean efficiency on each bottom BabyMOSS region against VCASB. The trend observed in (a) is also visible here, with some exceptions.

Figure 3.2: Mean efficiency on BabyMOSS regions against VCASB: (a) top regions, (b) bottom regions.

One may notice from Fig. 3.4, the top half-unit of the BabyMOSS has generally higher intrinsic thresholds, even for the same VCASB values applied to the bottom half-unit.

It is evident from Fig. 3.3 and even more clearly from Fig. 3.4, lower thresholds *do* result in larger efficiencies measured by the sensors, as can be understood through

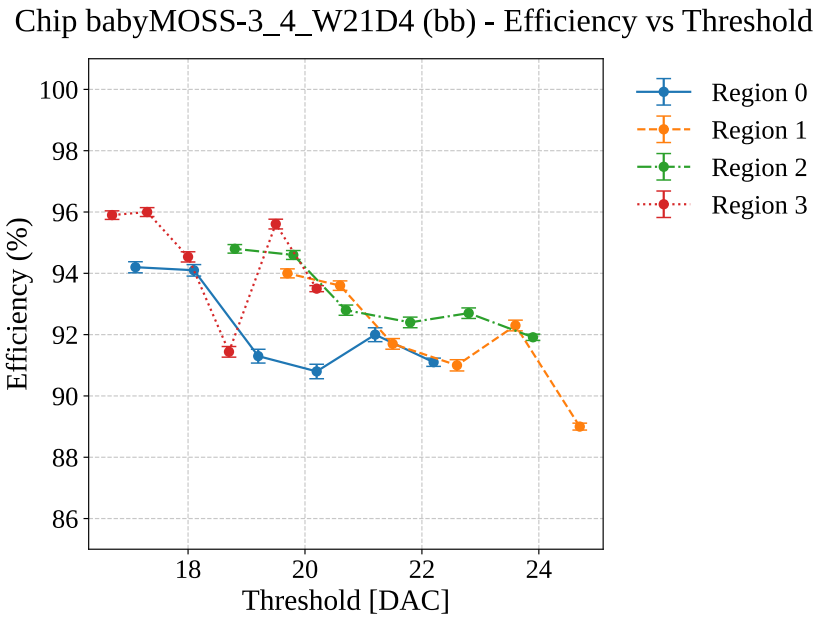

Figure 3.3: Mean efficiencies on each bottom BabyMOSS region against threshold.

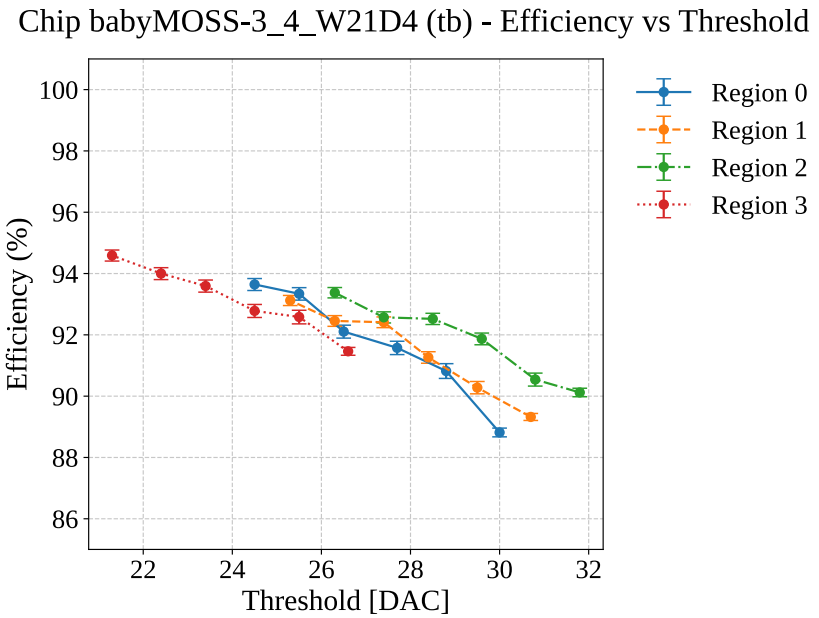

Figure 3.4: Mean efficiencies on each top BabyMOSS region against threshold.

the explanation in Sec. 2.3.1. Lower thresholds allow particles, which for any given reason deposit less charge into the pixel, to still be read. Since this indicates that the total number of hits on the pixel increases, then the efficiency should increase. This further confirms earlier assumptions and is consistent with other pixel detectors. The data points do not behave exactly the same way in translating the VCASB to threshold because different VCASBs resulted in different mean thresholds in each region when

laboratory measurements were conducted, which is to be expected.

Angle Dependency

As summarized in Sec. 1.1, a hit is registered by a pixel when the charge carriers, produced as a result of ionisation by the charged particle passing through the active layer, drift and are measured by the diodes. When the active layer is effectively thicker, as it is with angled measurements, a larger number of charge carriers are released, almost always ensuring a hit is read. It is then expected that the efficiency of such a sensor to increase to nearly 100% for a large angle.

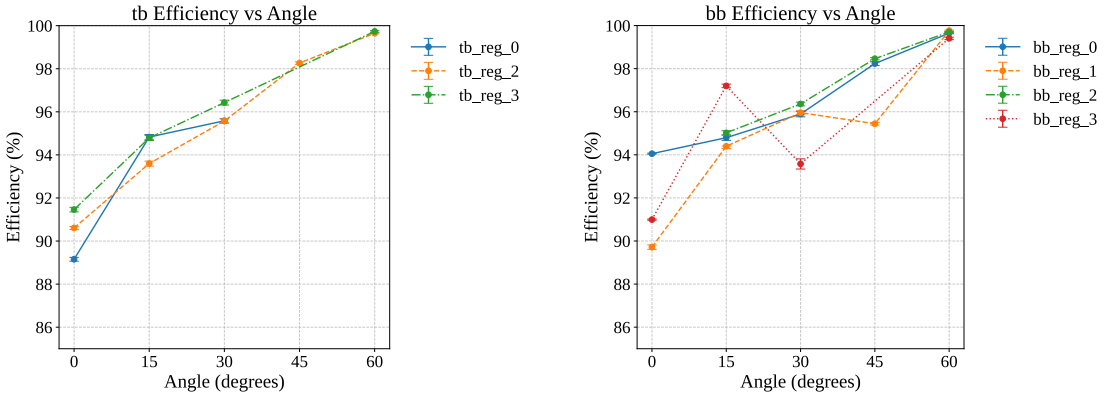

(a) Mean efficiency of each BabyMOSS region versus beam angle for the top half unit of the DUT.

(b) Mean efficiency of each BabyMOSS region versus beam angle for the bottom half unit of the DUT.

Figure 3.5: Changes in mean efficiency of BabyMOSS regions with respect to beam angle: (a) top half unit, (b) bottom half unit.

The mean efficiencies of each region of the BabyMOSS DUT against the different angles set in the DESY test beam are graphed in Figs 3.5a, 3.5b. It is clear that an assumption of increasing efficiency was correct, as one evidently sees an almost 100% efficiency at 60°. Some comparative data, more specifically that for `tb_reg_1` and some angle measurements for `tb_reg_0`, i.e. top region one and zero, is absent from the graph. This is due to the fact that top region one was deactivated during most of the data-taking due to an error. At larger angles, as mentioned, some regions needed to be aligned with neighbouring regions in order to preserve the maximum possible amount of events and therefore statistics, thus requiring a re-alignment when compared to the flat configuration.

3.2.2 Spatial Resolution

In order to accurately calculate the spatial resolution of any pixel detector or region of a pixel detector in this thesis, one must try to perfect the alignment and extract the residual distributions of the given sensor, so as to apply Eq. 3.3 with proper precision. The tracking uncertainty can be calculated using tools such as "The Telescope Optimiser" [27].

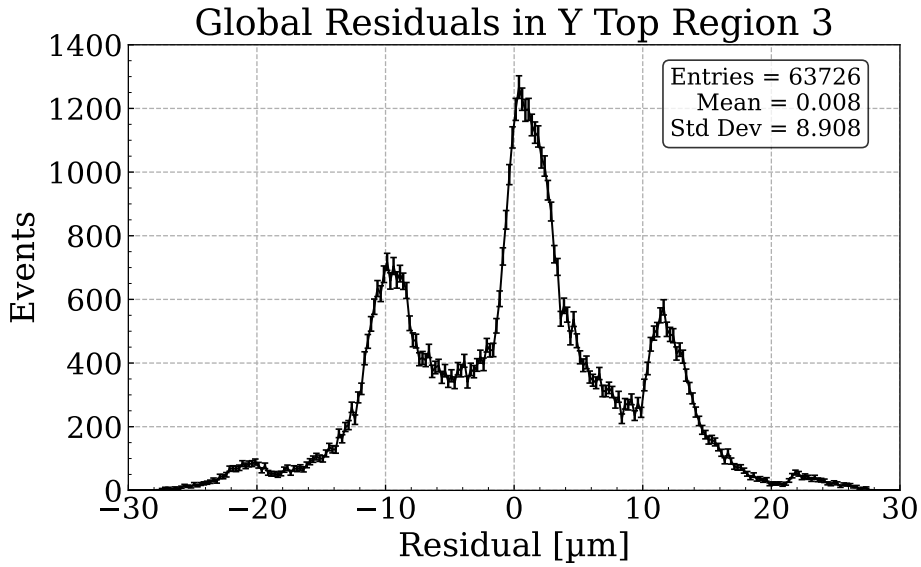

Figure 3.6: Residual distribution in global coordinates for Top Region 3 on the Baby-MOSS DUT in the Y-direction, i.e. in the row direction, along the columns. The three peaks seen here can be explained through pixel discretisation between detector layers, therefore implying good alignment.

An example of a well-aligned sensor is visualized in Fig. 3.6. There is a clear three-peak structure in the histogram, seemingly centered around the middle but not symmetric. This effect on the DUT residuals stems from the fact that the tracking algorithm requires hits on the reference telescope layers behind and in front of the DUT, then analyzing the tracks produced from these cluster hits to also have intersections at the DUT, in principle also requiring a hit on the DUT. As discussed in Sec. 2.1, any hit on any part of the pixels is then always geometrically shifted to the centre of the pixel. When the telescope and DUT are well aligned, the hit requirements cause a slight discretisation of possibilities of how shifted the residuals are, i.e., the residuals have higher densities at distances according to how shifted the individual pixels on each of the front or back layers are with respect to the middle DUT layers. A larger density at around 0 µm implies good alignment, when also observing $O(10\,\mu\text{m})$ shifts on the nearest layers. The same, yet weaker, effect can be identified near the edges of the distribution, corresponding to the layers at the ends of the telescope. It is to be noted that this effect is seen more starkly when employing the GBL tracking model rather than the Straight-Line tracking model, since the latter does not take multiple scattering into account and therefore fits particle tracks less to pixel edges and rather more often to pixel centres.

VCASB dependency

In addition to efficiency, the spatial resolution of the detectors is expected to improve with lower threshold values or, equivalently, higher VCASB values, as more particles are expected to be measured, therefore increasing the statistical information for the

residual values and distribution.

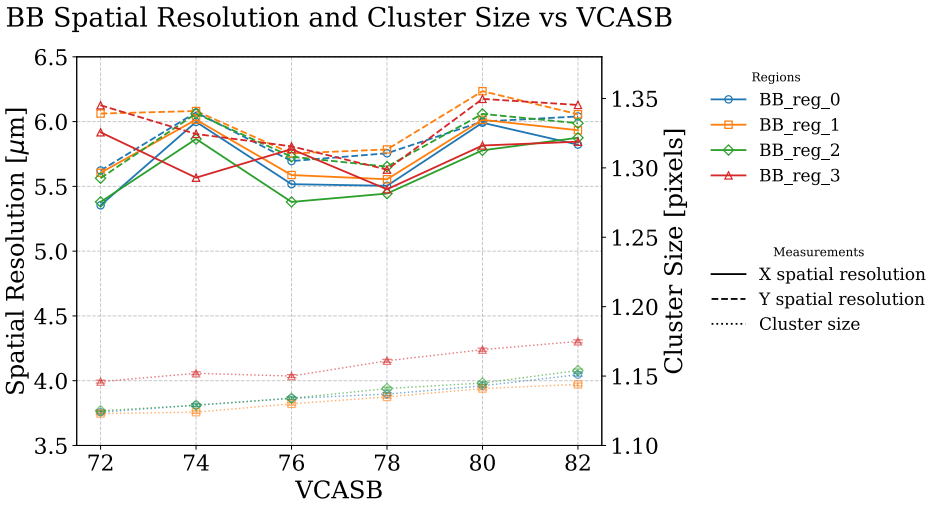

(a) Spatial resolution and cluster size in both plane directions (X and Y coordinates) against measured VCASB values for the bottom half-unit on the DUT.

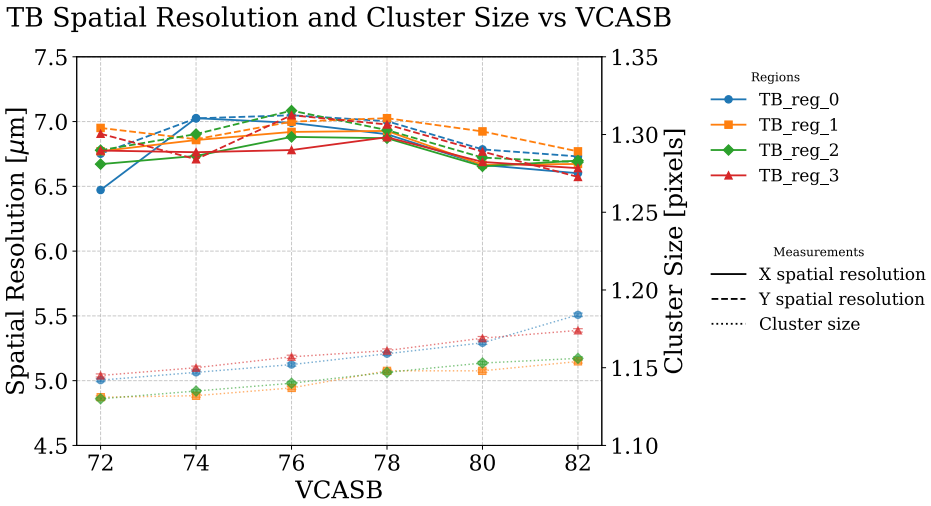

(b) Spatial resolution and cluster size in both plane directions (X and Y coordinates) against measured VCASB values for the top half-unit on the DUT.

Figure 3.7: Spatial resolution in both X and Y directions of each region on top and bottom half-units, as well as mean cluster sizes against VCASB.

As can be observed in Figs. 3.7a, 3.7b, the spatial resolution fluctuates with VCASB values, with the effect being most apparent for the bottom half-unit regions on the DUT. The expected trend of improvement mentioned above is comparatively more perceivable for the top half-unit regions, but yet only nearing larger VCASB values. It is unclear what the underlying factor for this is. A possibility could be that the alignment process is imperfect, producing large residual distributions due to misalignment.

The mean cluster sizes on each of the half-unit regions are also shown in Figs. 3.7. With larger VCASB values, the mean threshold values drop in each region, allowing for

a larger number of hits to be registered, in turn increasing the number of pixels that are fired for a given event. Thus, cluster sizes grow.

Angle Dependency

The spatial resolution for each region was calculated from the residual distributions. At larger incidence angles, the effective thickness of the active layer increases, leading to a larger number of pixels sharing charge from a single particle. This enhanced charge sharing improves the interpolation of the hit position, since the cluster centre can be reconstructed more precisely than the binary information from a single pixel. As a result, the spatial resolution improves for angled tracks compared to perpendicular ones.

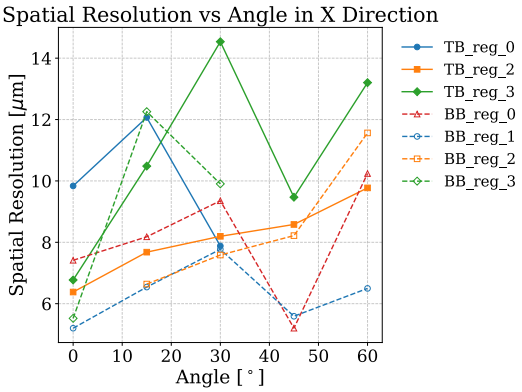

(a) Spatial resolutions of all regions in X direction against angle.

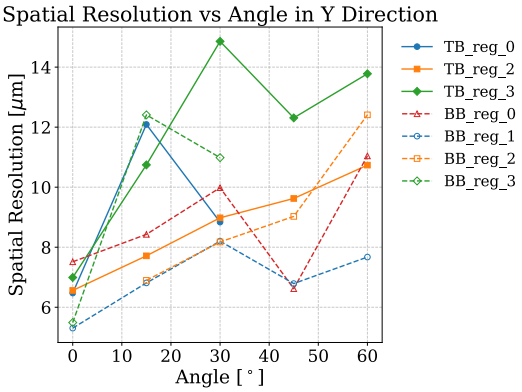

(b) Spatial resolutions of all regions in the Y direction against angle.

As can be seen in Fig. **??**, the spatial resolution does not seem to follow the expected decrease (improvement) with larger angles. The reason for this unexpected behaviour is unclear. One possible explanation could be the imperfection of the alignment procedure, but these results are still to be further investigated.

3.2.3 In-pixel Efficiency

In-pixel information allows one to determine many characteristics of the sensor on a pixel scale. Detection Efficiency, in particular, quantifies how well clustering is being measured, as well as highlighting if any hardware produces dead zones in a pixel.

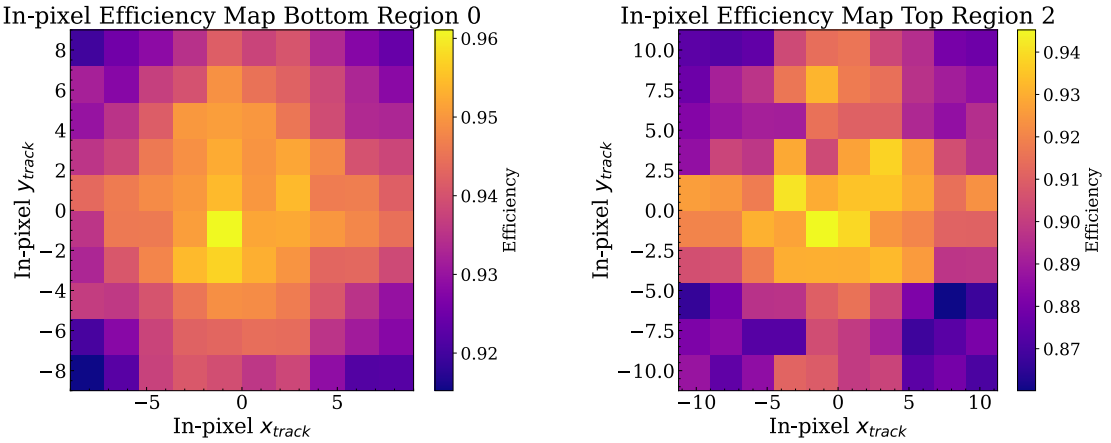

(a) In-pixel efficiency of the zeroth bottom region on the BabyMOSS DUT at 0°. The drops in efficiency at the corners of a pixel are due to charge sharing with pixel neighbours.

(b) In-pixel efficiency of the second top region on the BabyMOSS DUT at 0°. The charge sharing pattern is also to be seen here.

Figure 3.9: In-pixel efficiency of bottom (a) and top (b) regions of the BabyMOSS DUT at 0°.

3.3 APTS Results

Using a similar pipeline as described in Sec. 3.1.1, the APTS measurements from the DESY test beam were analysed for general performance, yet with no other special types of measurements other than having measurements with different back bias voltage, V_{BB}, values. The back bias voltage changes the depth of the depletion region in each pixel, thus affecting charge collection and with it the threshold values on a pixel, which in turn influences detection efficiency and spatial resolution.

Due to the reduced number of pixels on the APTS chips compared to BabyMOSS, the available statistics for the analysis were much lower, which affected both the alignment and the subsequent efficiency and spatial resolution measurements. For each run, two hundred thousand events were recorded and used for track fitting. After all alignment steps, only a few thousand tracks could be retained for the final efficiency and spatial resolution analysis.

3.3.1 Spatial Resolution

The larger depletion region volume and stronger magnetic field produced by larger V_{BB} are responsible for a reduction in charge diffusion and, therefore, charge sharing. This effect surprisingly has a negative effect on the spatial resolution of the sensor, as less charge sharing implies a loss of more accurate information on the ionizing particle. When charge is shared, it is then possible, based on charge depositions on each pixel, to determine a more exact position of the particle hit on the detector.

Due to a lack of large statistics for the measurements on APTS chips, as mentioned

in 3.3, no accurate residual distributions were able to be extracted from the APTS measurements, in turn not allowing for accurate spatial resolution calculations. Since one can calculate a statistical uncertainty with $u(n) = \frac{1}{\sqrt{n}}$, where n is the number of events, an accurate calculation of any characteristic would require one hundred times longer measurements.

3.3.2 Detection Efficiency

As mentioned in Sec. 3.3, detection efficiency is affected by V_{BB} values due to changes in the threshold. The mean efficiencies on each sensor at different V_{BB} values are listed in Tab. 3.1.

Table 3.1: Efficiencies of the APTS chips at different back-bias voltages V_{BB}. Note: APTS_AF25P_W22T06 contains a faulty pixel in the inner four-pixel matrix. For APTS_AF25P_W22T07, there is not enough statisticsal information to produce an accurate value for the detection efficiency.

V_{BB} [V]	APTS_AF25P_W22T06	APTS_AF25P_W22T07
0.0	$77.8^{+0.9}_{-0.9}$%	$28.5^{+1.9}_{-1.8}$%
-1.2	$97.2^{+0.3}_{-0.4}$%	–
-2.4	$98.3^{+0.2}_{-0.3}$%	–

The APTS measures signal amplitudes, allowing the corresponding distributions to be plotted, as can be seen in Fig. 3.10, which displays the expected Landau-like shape. Increasing the V_{BB} voltage strengthens the electric field within the sensor, which increases the signal for each deposited charge and effectively lowers the threshold in terms of electrons. Consequently, detection efficiency improves, as a smaller fraction of the low-amplitude tail of the distribution is suppressed by the threshold.

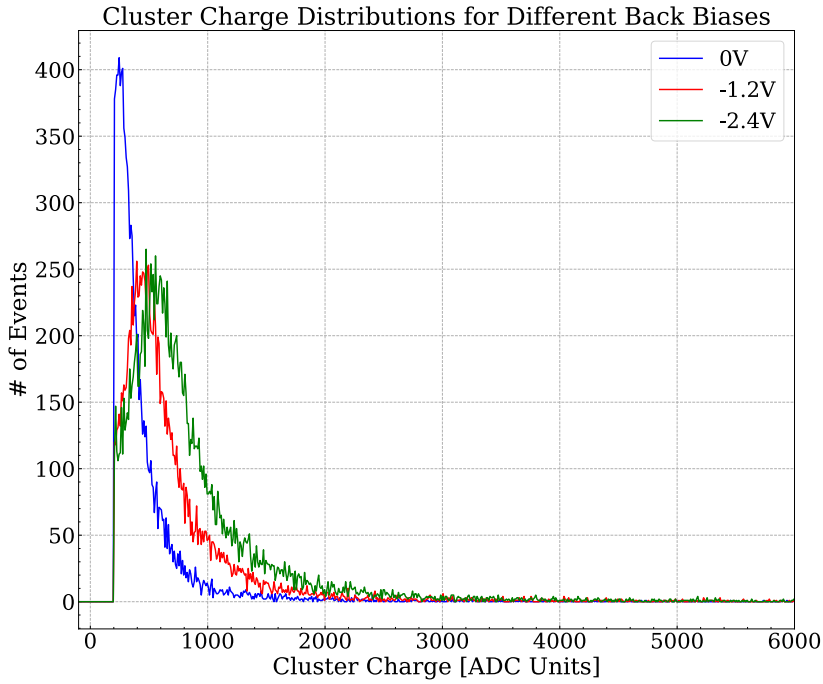

Figure 3.10: Cluster charge distributions for APTS_AF25P_W22T06 at a seed threshold of two hundred ADC units. There is a clear Landau-distribution to be seen.

4 Conclusion and Outlook

In this thesis, two different MAPS detectors, the BabyMOSS and APTS, were investigated, and their spatial resolution and efficiency were characterized as part of the research for the ITS3 upgrade and the new ALICE 3 detector.

Firstly, laboratory measurements of multiple BabyMOSS sensors were performed, namely threshold and FHR scans at different VCASB values. With this information, a reasonable basis for the optimal operational parameters of each of the chips was achieved, to execute further measurements at a DESY electron test beam with a momentum of 2.4 GeV/c, whereas an energy of 2.1 GeV/c was deduced to be more likely based on Geant4 simulation data for the telescope data at hand when taking multiple scattering at hand. Similarly, APTS data were taken during the DESY test beam as well.

In order to study the effects of threshold changes and effective active epitaxial layer thickness on spatial resolution and detection efficiency for BabyMOSS, data for the DUT of the same type at angles 0°, 15°, 30°, 45°, and 60° were obtained, as well as information for different VCASB values at 0°. For the APTS, apart from zero for both, two different V_{BB} values were applied on one of the chips during the test beam, applying DPTS triggering, where only particles that also passed through a DPTS are considered measured.

The comparative analysis of the BabyMOSS laboratory measurements was carried out by means of Python scripts automatising the analysis of the multiple BabyMOSS and producing comparative graphs from the computed values, therefore clarifying trends in the data. On the other hand, for the DESY test beam measurements, detection efficiency and spatial resolution, i.e., residual distribution calculation through alignment, were performed using the Corryvreckan test beam data analysis framework. From then on, the output information was presented against the changed variables in order to investigate the behaviour of the sensors when changing said variables.

The results from the angled measurements agreed with the assumption that the efficiency of a BabyMOSS detector would increase when particles are incoming at an angle. For a real proton or heavy-ion collision situation, as would be in ALICE 3 or after the installation of ITS3 into the current ALICE experiment, many particles take paths not initially perpendicular to the plane of a pixel. Therefore, good efficiencies could be expected, retaining almost all of the information on the paths, as well as charge collection.

Changing the VCASB value on a MAPS chip, in this case, BabyMOSS detectors, influences the threshold value on each pixel. Larger VCASB values lower the threshold, which in turn facilitates more particles to be detected, as lower charge values being deposited would still be large enough to go above the threshold. As such, more hits are registered by pixels, allowing more clusters to be measured and therefore be matched to tracks fitted on each detector layer, increasing efficiency. The in-pixel detection

efficiency provides charge-sharing information between pixels. When particles hit the edges of pixels, the charge is divided among said pixels, creating the cluster, then assigning it a center dependent on the amount of charge measured. This facilitates tracking the position of the particle passing through the detector.

The spatial resolution of the BabyMOSS was also investigated in relation to the change in VCASB values, with the results not showing a strong match with the expected trend of improvement with larger VCASB values, which would be a result of the reduced threshold values.

For the APTS measurements from the DESY test beam, the efficiencies of the chip at different back-bias voltage values were investigated, as the efficiency was expected to change with more charge per cluster. This increase is due to the strengthening of the electric field across the pixels as a result of the large back-bias values.

In conclusion, the presented investigation provides a clear investigation pipeline for MAPS sensors, which are to be characterised, as well as important information on the operating variables necessary for the best possible measurements. The studies presented in this thesis demonstrate that the assembled BabyMOSS-based telescope is suitable for the characterization of MAPS sensors, in particular the APTS. This capability is directly relevant for the study of large-pitch APTS prototypes planned for next year. The results obtained with this telescope, using the analysis pipeline developed in this work, will be critical for assessing the limits of MAPS pixel sizes and will inform the design of the ALICE 3 Outer Tracker sensor, which, once constructed, will constitute the largest MAPS detector in the world.

Acknowledgments

First of all, I would like to extend my gratitude to my supervisor, Henrik Fribert, for all the help, advice, and jokes. I am grateful to Prof. Laura Fabbietti as well for providing me with the opportunity to be a part of this group, as well as these projects.

I would also like to thank Berkin Ulukutlu, Lukas Lautner, and Dr. Roman Gernhäuser for offering their expertise and experience along the way, as well as the rest of the MAPSCrew. Finally, I thank my family and friends, especially my parents, for helping me even begin studying physics and pursue my goals, and my girlfriend, for encouraging me and supporting me in the process.

I acknowledge DESY (Hamburg, Germany), a member of the Helmholtz Association HGF, for the provision of experimental facilities. Parts of this research were carried out at the test beam line T22.

List of Figures

List of Tables

Bibliography

[1] E. Heijne, P. Jarron, A. Olsen, and N. Redaelli. "The silicon micropattern detector: a dream?" In: *Nuclear Instruments and Methods in Physics Research Section A: Accelerators, Spectrometers, Detectors and Associated Equipment* 273 (1988), pp. 615–619. DOI: 10.1016/0168-9002(88)90890-0

[2] R. Turchetta. "CMOS monolithic active pixel sensors (MAPS) for scientific applications". In: *9th Workshop on Electronics for LHC Experiments*. 2003. DOI: 10.5170/CERN-2003-006.28. URL: https://cds.cern.ch/record/712036

[3] E. R. Fossum. "CMOS Image Sensors: Electronic Camera-On-A-Chip". In: *IEEE Transactions on Electron Devices* 44.10 (2003), pp. 1689–1698

[4] M. Mager. "ALPIDE, the Monolithic Active Pixel Sensor for the ALICE ITS upgrade". In: *Nuclear Instruments and Methods in Physics Research Section A: Accelerators, Spectrometers, Detectors and Associated Equipment* 824 (2016). Frontier Detectors for Frontier Physics: Proceedings of the 13th Pisa Meeting on Advanced Detectors, pp. 434–438. DOI: 10.1016/j.nima.2015.09.057. URL: https://www.sciencedirect.com/science/article/pii/S0168900215011122

[5] K. Aamodt et al. "The ALICE experiment at the CERN LHC". In: *JINST* 3 (2008), S08002. DOI: 10.1088/1748-0221/3/08/S08002

[6] B. Abelev and A. Collaboration. "Technical Design Report for the Upgrade of the ALICE Inner Tracking System". In: *Journal of Physics G: Nuclear and Particle Physics* 41.8 (2014), p. 087002. DOI: 10.1088/0954-3899/41/8/087002

[7] G. Dellacasa et al. "ALICE: Technical design report of the time projection chamber". In: (Jan. 2000)

[8] F. Sauli. "GEM: A new concept for electron amplification in gas detectors". In: *Nuclear Instruments and Methods in Physics Research Section A: Accelerators, Spectrometers, Detectors and Associated Equipment* 386.2 (1997), pp. 531–534. DOI: https://doi.org/10.1016/S0168-9002(96)01172-2. URL: https://www.sciencedirect.com/science/article/pii/S0168900296011722

[9] H. Bethe and J. Ashkin. "Experimental Nuclear Physics". In: *Experimental Nuclear Physics*. Ed. by E. Segrè. New York: J. Wiley, 1953, p. 253

[10] A. Collaboration. *Technical Design Report for the ALICE Inner Tracking System 3 – ITS3: A bent wafer–scale monolithic pixel detector*. Tech. rep. Geneva: CERN, 2024. URL: https://cds.cern.ch/record/2890181

[11] A. Sturniolo. "MLR1: CMOS MAPS technology validation for ALICE ITS3". In: *Nuovo Cimento C* 48.3 (2025), p. 157. DOI: 10.1393/ncc/i2025-25157-3. URL: https://cds.cern.ch/record/2936835

[12] G. A. Rinella et al. "Characterization of analogue Monolithic Active Pixel Sensor test structures implemented in a 65 nm CMOS imaging process". In: *Nuclear Instruments and Methods in Physics Research Section A: Accelerators, Spectrometers, Detectors and Associated*

Equipment 1069 (2024), p. 169896. DOI: 10.1016/j.nima.2024.169896. URL: https://www.sciencedirect.com/science/article/pii/S0168900224008222

[13] G. Aglieri Rinella et al. "Digital pixel test structures implemented in a 65 nm CMOS process". In: *Nuclear Instruments and Methods in Physics Research Section A: Accelerators, Spectrometers, Detectors and Associated Equipment* 1056 (2023), p. 168589. DOI: https://doi.org/10.1016/j.nima.2023.168589. URL: https://www.sciencedirect.com/science/article/pii/S016890022300579X

[14] O. Aberle et al. *High-Luminosity Large Hadron Collider (HL-LHC): Technical design report*. CERN Yellow Reports: Monographs. Geneva: CERN, 2020. DOI: 10.23731/CYRM-2020-0010. URL: https://cds.cern.ch/record/2749422

[15] A. Collaboration. *Letter of intent for ALICE 3: A next-generation heavy-ion experiment at the LHC*. 2022. arXiv: 2211.02491 [physics.ins-det]. URL: https://arxiv.org/abs/2211.02491

[16] A. Dainese and A. D. Mauro. *Scoping document for the ALICE 3 detector*. Tech. rep. Geneva: CERN, 2025. URL: https://cds.cern.ch/record/2925455

[17] H. Xiao. "Introduction to Integrated Circuit Fabrication". In: *Introduction to Semiconductor Manufacturing Technology (2nd Edition)*. SPIE, 2012. URL: https://app.knovel.com/hotlink/pdf/id:kt00BXRTS1/introduction-semiconductor/introduction-integrated

[18] P. V. Leitao et al. "Development of a Stitched Monolithic Pixel Sensor prototype (MOSS chip) towards the ITS3 upgrade of the ALICE Inner Tracking system". In: *Journal of Instrumentation* 18.01 (2023), p. C01044. DOI: 10.1088/1748-0221/18/01/C01044. URL: https://dx.doi.org/10.1088/1748-0221/18/01/C01044

[19] A. I. WP3. *MOSS User Manual*. 2025. URL: https://gitlab.cern.ch/groups/alice-its3-wp3/moss-testing/-/wikis/Moss%20user%20manual (visited on 09/09/2025)

[20] W. Snoeys et al. "A process modification for CMOS monolithic active pixel sensors for enhanced depletion, timing performance and radiation tolerance". In: *Nuclear Instruments and Methods in Physics Research Section A: Accelerators, Spectrometers, Detectors and Associated Equipment* 871 (2017), pp. 90–96. DOI: https://doi.org/10.1016/j.nima.2017.07.046. URL: https://www.sciencedirect.com/science/article/pii/S016890021730791X

[21] M. Buckland. *First measurements with monolithic active pixel test structures produced in a 65 nm CMOS process*. 2023. arXiv: 2309.14814 [physics.ins-det]. URL: https://arxiv.org/abs/2309.14814

[22] Y. Liu. *EUDAQ2 User Manual*. Tech. rep. Geneva: CERN, 2018. URL: https://cds.cern.ch/record/2314266 (visited on 09/09/2025)

[23] M. Williams, S. Spannagel, and J. Kröger. *Corryvreckan User Manual, Version v2.0-2104-gc2e5798*. Tech. rep. CERN, Sept. 2025. URL: https://project-corryvreckan.web.cern.ch/project-corryvreckan/

[24] C. Kleinwort. "General broken lines as advanced track fitting method". In: *Nuclear Instruments and Methods in Physics Research Section A: Accelerators, Spectrometers, Detectors and Associated Equipment* 673 (May 2012), pp. 107–110. DOI: 10.1016/j.nima.2012.01.024. URL: http://dx.doi.org/10.1016/j.nima.2012.01.024

[25] S. Navas and P. D. Group. In: *Physical Review D* 110 (2024). Chapter 40, p. 030001

[26] S. Agostinelli et al. "GEANT4 - A Simulation Toolkit". In: *Nucl. Instrum. Meth. A* 506 (2003), pp. 250–303. DOI: 10.1016/S0168-9002(03)01368-8

[27] M. Mager. *The Telescope Optimiser*. 2016. URL: https://mmager.web.cern.ch/telescope/tracking.html (visited on 09/09/2025)